



**AFRL-RX-WP-TR-2010-4083**

**COLLABORATIVE RESEARCH AND DEVELOPMENT  
(CR&D)**

**Delivery Order 0026: Tribological Modeling**

**Young Sup Kang**

**Universal Technology Corporation**

**AUGUST 2006**

**Final Report**

**Approved for public release; distribution unlimited.**

*See additional restrictions described on inside pages*

**STINFO COPY**

**AIR FORCE RESEARCH LABORATORY  
MATERIALS AND MANUFACTURING DIRECTORATE  
WRIGHT-PATTERSON AIR FORCE BASE, OH 45433-7750  
AIR FORCE MATERIEL COMMAND  
UNITED STATES AIR FORCE**

## NOTICE AND SIGNATURE PAGE

Using Government drawings, specifications, or other data included in this document for any purpose other than Government procurement does not in any way obligate the U.S. Government. The fact that the Government formulated or supplied the drawings, specifications, or other data does not license the holder or any other person or corporation; or convey any rights or permission to manufacture, use, or sell any patented invention that may relate to them.

This report was cleared for public release by the Air Force Research Laboratory Wright Site (AFRL/WS) Public Affairs Office (PAO) and is available to the general public, including foreign nationals. Copies may be obtained from the Defense Technical Information Center (DTIC) (<http://www.dtic.mil>).

AFRL-RX-WP-TR-2010-4083 HAS BEEN REVIEWED AND IS APPROVED FOR PUBLICATION IN ACCORDANCE WITH THE ASSIGNED DISTRIBUTION STATEMENT.

\*//Signature//

---

MARK N. GROFF  
Project Engineer  
Business Operations Branch  
Integration and Operations Division

//Signature//

---

KENNETH A. FEESER  
Chief  
Business Operations Branch  
Integration and Operations Division

This report is published in the interest of scientific and technical information exchange, and its publication does not constitute the Government's approval or disapproval of its ideas or findings.

\*Disseminated copies will show “//Signature//” stamped or typed above the signature blocks.

| <b>REPORT DOCUMENTATION PAGE</b>  |                                    |                                     |   |   | <i>Form Approved</i><br>OMB No. 0704-0188                         |  |
|---|------------------------------------|-------------------------------------|---|---|---|--|
| The public reporting burden for this collection of information is estimated to average 1 hour per response, including the time for reviewing instructions, searching existing data sources, gathering and maintaining the data needed, and completing and reviewing the collection of information. Send comments regarding this burden estimate or any other aspect of this collection of information, including suggestions for reducing this burden, to Department of Defense, Washington Headquarters Services, Directorate for Information Operations and Reports (0704-0188), 1215 Jefferson Davis Highway, Suite 1204, Arlington, VA 22202-4302. Respondents should be aware that notwithstanding any other provision of law, no person shall be subject to any penalty for failing to comply with a collection of information if it does not display a currently valid OMB control number. <b>PLEASE DO NOT RETURN YOUR FORM TO THE ABOVE ADDRESS.</b> |                                    |                                     |   |   |   |  |
| <b>1. REPORT DATE (DD-MM-YY)</b><br>August 2006   |                                    | <b>2. REPORT TYPE</b><br>Final      |   | <b>3. DATES COVERED (From - To)</b><br>17 May 2004 – 30 June 2006                   |   |  |
| <b>4. TITLE AND SUBTITLE</b><br>COLLABORATIVE RESEARCH AND DEVELOPMENT (CR&D)<br>Delivery Order 0026: Tribological Modeling   |                                    |                                     |   | <b>5a. CONTRACT NUMBER</b><br>F33615-03-D-5801-0026                                 |   |  |
|   |                                    |                                     |   | <b>5b. GRANT NUMBER</b>   |   |  |
|   |                                    |                                     |   | <b>5c. PROGRAM ELEMENT NUMBER</b><br>62102F   |   |  |
| <b>6. AUTHOR(S)</b><br>Young Sup Kang   |                                    |                                     |   | <b>5d. PROJECT NUMBER</b><br>4349   |   |  |
|   |                                    |                                     |   | <b>5e. TASK NUMBER</b><br>L0  |   |  |
|   |                                    |                                     |   | <b>5f. WORK UNIT NUMBER</b><br>4349L0VT   |   |  |
| <b>7. PERFORMING ORGANIZATION NAME(S) AND ADDRESS(ES)</b><br>Universal Technology Corporation<br>1270 North Fairfield Road<br>Dayton, OH 45432-2600   |                                    |                                     |   | <b>8. PERFORMING ORGANIZATION REPORT NUMBER</b><br>S-531-026                        |   |  |
| <b>9. SPONSORING/MONITORING AGENCY NAME(S) AND ADDRESS(ES)</b><br>Air Force Research Laboratory<br>Materials and Manufacturing Directorate<br>Wright-Patterson Air Force Base, OH 45433-7750<br>Air Force Materiel Command<br>United States Air Force   |                                    |                                     |   | <b>10. SPONSORING/MONITORING AGENCY ACRONYM(S)</b><br>AFRL/RXOB                     |   |  |
|   |                                    |                                     |   | <b>11. SPONSORING/MONITORING AGENCY REPORT NUMBER(S)</b><br>AFRL-RX-WP-TR-2010-4083 |   |  |
| <b>12. DISTRIBUTION/AVAILABILITY STATEMENT</b><br>Approved for public release; distribution unlimited.  |                                    |                                     |   |   |   |  |
| <b>13. SUPPLEMENTARY NOTES</b><br>PAO Case Number: AFRL/WS 07-0151; Clearance Date: 24 Jan 2007.<br>Research concluded in 2006.   |                                    |                                     |   |   |   |  |
| <b>14. ABSTRACT</b><br>This research in support of the Air Force Research Laboratory Materials and Manufacturing Directorate was conducted from 19 May 2006 through 31 January 2008. This task developed and used computer models of electron beam transmission through complex semiconductor heterostructures to determine the interface compositions in real images, and to study how growth and/or processing conditions affect the layers and interfaces. The techniques and models developed, as well as the results of applications of these models to AFRL/MLPS-provided semiconductor samples are reported.   |                                    |                                     |   |   |   |  |
| <b>15. SUBJECT TERMS</b>  |                                    |                                     |   |   |   |  |
| <b>16. SECURITY CLASSIFICATION OF:</b>  |                                    |                                     | <b>17. LIMITATION OF ABSTRACT:</b><br>SAR | <b>18. NUMBER OF PAGES</b><br>64  | <b>19a. NAME OF RESPONSIBLE PERSON (Monitor)</b><br>Mark N. Groff |  |
| <b>a. REPORT</b><br>Unclassified  | <b>b. ABSTRACT</b><br>Unclassified | <b>c. THIS PAGE</b><br>Unclassified |   |   | <b>19b. TELEPHONE NUMBER (Include Area Code)</b><br>N/A           |  |

## Table of Contents

|   | <u>Page</u> |
|---|-------------|
| List of Figures .....   | iv          |
| List of Tables .....  | vi          |
| 1.0 SUMMARY .....   | 1           |
| 2.0 INTRODUCTION.....   | 1           |
| 3.0 A STUDY OF STRESS DISTRIBUTION IN LAYERED AND GRADIENT<br>TRIBOLOGICAL COATINGS .....                               | 4           |
| 3.1 Introduction.....   | 4           |
| 3.2 Description of the Layered and Gradient Ti/TiC Coating System.....  | 6           |
| 3.3 ABAQUS Finite Element Model .....   | 8           |
| 3.4 Results and Discussion .....  | 10          |
| 3.5 Summary and Conclusion .....  | 27          |
| 4.0 NANOINDENTATION AND FINITE ELEMENT ANALYSIS OF MULTILAYERED<br>AND FUNCTIONALLY GRADIENT TRIBOLOGICAL COATINGS..... | 27          |
| 4.1 Introduction.....   | 27          |
| 4.2 Functionally Gradient (FG) Multilayered Tribological Coating.....   | 28          |
| 4.2.1 Nanoindentation.....  | 29          |
| 4.3 Results and Discussion .....  | 31          |
| 4.3.1 Yield Strength Calculation Procedure.....   | 31          |
| 4.3.2 Nanoindentation for Ti/TiC/DLC Coating Material Properties.....   | 36          |
| 4.3.3 Finite Element Analysis Model Results.....  | 39          |
| 4.4 Summary and Conclusion .....  | 51          |
| 5.0 REFERENCES .....  | 52          |



## List of Figures

| <u>Figure</u>   | <u>Page</u> |
|---|-------------|
| 3.1 Multilayered and functionally gradient Ti/TiC/DLC coating system that shows the gradual composition variation across the thicknesses of the layers. ....  | 6           |
| 3.2 Schematic of indentation with a rigid spherical indenter on multilayered semi-infinite medium. ....   | 7           |
| 3.3 Schematic of functionally gradient Ti/TiC coating design with compositional and mechanical properties variation. ....   | 7           |
| 3.4. Schematic of three dimensional finite element analysis model developed for the nanoindentation with a rigid spherical indenter tip on multilayered and functionally gradient coating system. ....  | 9           |
| 3.5 Hertzian contact pressure distribution on semi-infinite medium indented by a rigid spherical indenter; (a) normalized contact pressure distribution by finite element solution for $W = 0.0035$ N and (b) contact pressure distributions at the center of contact along the plane of symmetry obtained by finite element and analytical solutions. .... | 11          |
| 3.6 Von Mises stress distribution in semi-infinite medium indented by a rigid spherical indenter for normal load, $W = 0.0035$ N ( $\mu = 0.0$ ); (a) perspective view of normalized von Mises stress on the plane of symmetry and (b) contour plot of normalized von Mises stress on the plane of symmetry. ....   | 12          |
| 3.7 Analytical and finite element solutions of normalized stresses in the semi-infinite medium due to the normal load at the surface ( $\mu = 0$ ). ....  | 14          |
| 3.8 Analytical and finite element solutions of the stresses in a layered and gradient coating system due to normal load at the surface ( $\mu = 0.0$ ). ....  | 14          |
| 3.9 Von Mises stress distribution in layered and gradient Ti/TiC coating system indented by a rigid spherical indenter for indentation load, $W = 0.0035$ N ( $\mu = 0.0$ ); (a) perspective view of normalized von Mises stress on the plane of symmetry and (b) contour plot of normalized von Mises stress on the plane of symmetry. ....                | 15          |
| 3.10 Effect of coating design on von Mises stress in (a) monolayer coating system and (b) layered and gradient coating system for normal load, $W = 0.0035$ N ( $\mu = 0.0$ ). ....   | 16          |
| 3.11 Contour plots of von Mises stress in layered and gradient coating system indented by a rigid spherical indenter for normal load; (a) $W = 4.4 \times 10^{-4}$ N, (b) $0.0035$ N, (c) $0.0119$ N, and (d) $0.0283$ N. ....  | 17          |
| 3.12 Von Mises stress distribution in layered and gradient coating system indented by a rigid spherical indenter for $Ti_{30}C_{70}$ coating thickness, $500$ nm, normal load, $4.4 \times 10^{-4}$ N, and friction coefficient, $0.0$ ; (a) von Mises stress distribution and (b) contour plot of von Mises stress. ....                                   | 19          |
| 3.13 Effect of top $Ti_{30}C_{70}$ coating thickness on von Mises stress in layered and gradient coating system for various $Ti_{30}C_{70}$ thicknesses ( $W = 0.0035$ and $\mu = 0.0$ ). ....  | 20          |
| 3.14 Effect of top coating thickness on contact pressure distribution on layered and gradient coating system indented by a rigid spherical indenter ( $W = 0.0035$ N, $\mu = 0.0$ ). ....   | 21          |

|      |   |    |
|------|---|----|
| 3.15 | Effect of applied load on von Mises stress in layered and gradient coating system indented by a rigid spherical indenter for various normal loads ( $\text{Ti}_{30}\text{C}_{70} = 350 \text{ nm}$ , $\mu = 0.0$ ).....   | 23 |
| 3.16 | Effect of bond layer materials on von Mises stress in layered and gradient coating system for $W = 0.0035 \text{ N}$ and $\mu = 0.0$ .....  | 23 |
| 3.17 | Effect of friction coefficient on von Mises stress in layered and gradient coating system for normal load (a) $W = 4.4 \times 10^{-4} \text{ N}$ and (b) $W = 0.0283$ ( $\text{Ti}_{30}\text{C}_{70} = 350 \text{ nm}$ ). ....  | 24 |
| 3.18 | Effect of plasticity on von Mises stress in layered and gradient coating system for $\text{Ti}_{30}\text{C}_{70} = 350 \text{ nm}$ , $W = 0.15 \text{ N}$ , and $\mu = 0.0$ ; (a) contour plot of von Mises stress on the plane of symmetry and (b) stress profile of von Mises stress along the centerline of the contact for elastic material properties and elastic-plastic material properties..... | 26 |
| 4.1  | Finite element analysis (FEA) model of the nanoindentation simulation with a conical indenter tip for the coating samples. ....   | 30 |
| 4.2  | Load vs. displacement curves for elastic deformation and elastic-plastic deformation from nanoindentation experiment respectively.....  | 31 |
| 4.3  | Nanoindentation results for $\text{SiO}_2$ ; (a) hardness vs. displacement plot, (b) modulus of elasticity vs. displacement plot, (c) load vs. displacement plot, and (d) load vs. displacement plot for experimental results and FEA results.....  | 33 |
| 4.4  | Nanoindentation results for 440C stainless steel; (a) load vs. displacement plot and (b) comparison of load vs. displacement plot between average experimental results and best-fit simulation results. ....  | 35 |
| 4.5  | Schematic of nanoindentation with a Berkovich indenter tip on coating samples such as $\text{Ti}$ , $\text{Ti}_{1-x}\text{C}_x$ , and DLC on 440C stainless steel to measure the material properties. ....  | 36 |
| 4.6  | Nanoindentation results for $\text{Ti}_{53}\text{C}_{47}$ coating; (a) hardness vs. displacement plot, (b) modulus of elasticity vs. displacement plot, (c) load vs. displacement plot during loading and unloading stages, and (d) comparison of measured average load vs. displacement curve and best-fit load vs. displacement curve from experiments and FEA simulations, respectively. ....        | 38 |
| 4.7  | Schematic of the functionally gradient $\text{Ti/TiC/DLC}$ coating design with variation of composition, dimension, and mechanical properties. ....   | 39 |
| 4.8  | (a) Schematic of nanoindentation on multilayered coating system with a spherical indenter tip, (b) two dimensional axi-symmetric finite element analysis model developed for nanoindentation simulation on a functionally gradient $\text{Ti/TiC/DLC}$ multilayered coating system with a spherical indenter tip. ....  | 40 |
| 4.9  | Effect of multilayered FG $\text{Ti/TiC/DLC}$ coating system on von Mises stress distribution for the indentation depth, $\delta = 50 \text{ nm}$ , and coefficient of friction, $\mu = 0.0$ . ....   | 41 |
| 4.10 | Contour plots of von Mises stresses distribution generated inside the multilayered FG $\text{Ti/TiC/DLC}$ coating system from the FEA model at various indentation depths; (a) $\delta = 40 \text{ nm}$ , (b) $\delta = 80 \text{ nm}$ , (c) $\delta = 120 \text{ nm}$ , and (d) $\delta = 160 \text{ nm}$ . ....   | 43 |

|      |  |    |
|------|--|----|
| 4.11 | (a) Von Mises stress distribution on the plane of symmetry generated inside the multilayered FG Ti/TiC/DLC coating system for the indentation depth, $\delta = 80$ nm and coefficient of friction, $\mu = 0.0$ and (b) contour plot of von Mises stress distribution. ....                     | 44 |
| 4.12 | Effect of applied load on von Mises stresses profiles along the depth direction at the center of the contact at various indentation depths for friction coefficient, $\mu = 0.0$ ; (a) $\delta = 40$ nm, (b) $\delta = 80$ nm, (c) $\delta = 120$ nm, and (d) $\delta = 160$ nm. ....          | 46 |
| 4.13 | Contour plots of equivalent plastic strain distribution generated on the plane of symmetry inside the multilayered FG Ti/TiC/DLC coating system at various indentation depths; (a) $\delta = 40$ nm, (b) $\delta = 80$ nm, (c) $\delta = 120$ nm, and (d) $\delta = 160$ nm. ....              | 48 |
| 4.14 | Contour plots of residual von Mises stress distribution generated inside multilayered FG Ti/TiC/DLC coating system after the unloading of nano indenter tip from various indentation depths; (a) $\delta = 40$ nm, (b) $\delta = 80$ nm, (c) $\delta = 120$ nm, and (d) $\delta = 160$ nm. ... | 49 |
| 4.15 | Effect of coating system design on von Mises stress distribution generated inside the coating system for the contact condition, $\delta = 200$ nm and $\mu = 0.0$ . ....   | 51 |

### List of Tables

| <u>Table</u>  | <u>Page</u> |
|---|-------------|
| 3.1 Contact conditions. ....  | 8           |
| 3.2 Material properties for bond layers. ....   | 22          |
| 4.1 Mechanical material properties such as modulus of elasticity (E) and hardness (H) for TiC/DLC coating samples. .... | 37          |

## **1.0 SUMMARY**

The primary objective of this study is to understand the fundamental mechanisms of interacting coated bodies through the tribological modeling and to develop optimized coating systems for severe contact applications. Ultimately the tribological modeling provides guidelines for the design and materials development of tribological coating systems in the future.

The emphasis of this investigation has been made on the development of numerical models to study the stress distribution and elastic plastic deformation generated inside the multilayered functionally gradient coating systems developed for the heavy load and scratch resistant applications. Finite element analysis (FEA) models were developed for the two dimensional and three dimensional contact problems. A widely used commercial software ABAQUS/Standard with ABAQUS/CAE pre and post processors was used for the development of FEA models. The project was divided into two parts: (i) stress modeling and (ii) nanoindentation and deformation modeling.

The first part of the study was focused on the study of stress distribution in layered and gradient tribological coating system. The critical parameters such as coating thickness, composition, applied load, material properties, and friction were identified and investigated for their effects on stress distribution inside the layered and gradient tribological coating system.

Aside from the mechanical stress modeling of the coating system, experimental nanoindentation technique in connection with FEA model simulation was also used to measure and calculate the material properties such as hardness, modulus of elasticity, and yield strength of the coating materials. Therefore, the second part of the study was focused on the material properties measurement and calculation by the aid of nanoindentation experiment in connection with FEA model simulation and the study of elastic plastic deformation inside the multilayered functionally gradient Ti/TiC/DLC coating system using the measured material properties.

## **2.0 INTRODUCTION**

When two bodies are in contact with relative motion while supporting load, stress and deformation fields are generated below the contact surface. The service life of machine components is major concern to the users and it is greatly influenced by the friction and wear characteristics of the contacting surfaces. Tribological behavior of the mating surfaces can be significantly improved by depositing thin hard coatings on them. Thin layer coatings such as TiN, TiC, CrN, and TiCN deposited on the contacting surfaces have been developed for various

applications to reduce the friction and wear of engineering components that experience severe operating conditions. Recently, diamond like carbon (DLC) coatings were recognized as wear protective coatings since amorphous DLC materials have the unique combination of high hardness, low friction and low wear. Although DLC coatings have the superior friction and wear characteristics to the conventional thin layer coatings, DLC coatings deposited on soft steel substrates have some disadvantages such as residual compressive stress and poor adhesion strength.

Lyubimov et al. [1] found that interfaces between layers are the prime locations for the film failure, e.g. by an interface crack growth, because of the considerable mechanical property differences at the interfaces. Voevodin et al. [2] showed that DLC coatings on steel substrates have the application limitations such as contact pressure (below 1 GPa) and coating thickness (below 0.5  $\mu\text{m}$ ) in order to avoid the coating failure, i.e. brittle fracture and delamination, at the coating/substrate interfaces due to significant material property differences. The limitations of DLC coatings were overcome by applying multilayer design concepts to the coating system. Voevodin et al. [3] proposed the several design concepts for the architecture of multilayer coatings to improve the limitations of the DLC coatings. They suggested the functionally gradient (FG) Ti/TiC/DLC coatings increase the load support and adhesion of the DLC coatings while maintaining low friction at the contacting surfaces. In such coatings, the composition and hardness vary gradually from the substrate to DLC, avoiding drastic variations in material properties. In addition, Voevodin et al. [4] developed the optimized design of hard coatings using the multilayer and FG approach experimentally. They found that the design architecture provided the gradual increase of the hardness from the substrate to DLC coating and substantially increased the adhesion of DLC coating.

Intelligent design of multilayered and FG coating systems requires a thorough understanding of layer architecture, chemistry and mechanical properties. Lyubimov et al. [1] concluded that the optimal choice of thickness, combination, and deposition conditions of layers should consider their stress state to prevent failure of multilayered coating systems. Therefore, it is of significant importance to analyze the stress distribution of the multilayered and gradient coatings and substrate through the development of finite element analysis models to identify the critical parameters that constrain the deformation and subsurface stresses of coating systems caused by normal contact conditions and to understand the failure mechanism of the coating

systems. In addition, to develop the numerical models accurately, the material properties such as hardness, modulus of elasticity, and yield strength need to be measured and calculated for each thin coating material. Due to the thickness of the thin coatings, conventional tensile test cannot be performed to generate the stress strain relationship for each coating material. One of the most widely used methods to measure the material properties for thin coating materials is the nanoindentation developed for characterizing thin coatings and layers mechanically because nanoindentation of thin coatings provides a relatively simple approach to quantify the mechanical properties of thin coatings. Due to the thickness of the thin coatings, only shallow indentation depth is allowed to extract the measurement data from the thin coating systems. From the nanoindentation of coating systems, the load vs. indentation depth curves are obtained and analyzed to determine properties such as modulus of elasticity and hardness. The measured and calculated material properties are used as inputs to the finite element analysis (FEA) models to study stress distribution and corresponding the elastic-plastic deformation behavior of the coating systems.

This present study focuses on the study of stress distribution and elastic plastic deformation on the multilayered and functionally gradient coating systems developed at the Air Force Research Laboratory. Therefore, the elastic plastic finite element analysis model has been developed for the multilayered and functionally gradient coating systems due to the nonlinear nature of the coating system using a commercial software ABAQUS/Standard. The FEA model has been used to understand the mechanisms involved in tribological contacts for a wide range of material properties, coating thickness, composition, applied load, and friction. Also, the FEA model has been used to determine the stress distribution in the multilayered FG tribological coating system and examine the elastic plastic deformation of the coating systems during nanoindentation. Nanoindentation experiments were conducted to measure the material properties such as hardness and modulus of elasticity for each coating material. In addition, nanoindentation FEA simulation in connection with the nanoindentation experiment was performed to calculate the yield strength of each coating material. The ultimate goal of this study is to develop optimized multilayered FG coating systems for high adhesion and scratch resistant applications. Further, the study is to provide the design guidelines for coating design and material development in the future.

### **3.0 A STUDY OF STRESS DISTRIBUTION IN LAYERED AND GRADIENT TRIBOLOGICAL COATINGS**

#### **3.1 Introduction**

Since the early 1950s, most of the early works were focused on developing the mathematical formulations and analytical solutions for the plain strain contact problems such as the elastic deformation of the layered media. Meijers [5] proposed mathematical formulations for the contact problem of a rigid cylinder pressed on an elastic layered media using asymptotic solutions. Satisfactory solution for all values of  $c/b$  (half width of contact area/layer thickness) and for Poisson's ratio between 0.0 and 0.5 was obtained for thin and thick layers. In 1970s, numerical analysis for the plain strain contact problems was performed by many researchers to avoid the mathematical complexity. Gupta and Walowit [6] developed a mathematic formulation for the normal contact of layered elastic solids using Fourier transform approach of Airy stress function. Numerical solutions of contact pressure and size of contact zone for a wide range of layer thickness were determined. Chiu and Hartnett [7] solved three dimensional counterformal contact problems involving layered solids using the generalized Boussinesq solution. King and O'Sullivan [8] developed a two dimensional quasi-static model to determine the stress field in layered elastic half-space under combined normal and sliding cylindrical contact. O'Sullivan and King [9] extended the two dimensional model to the full three dimensional model to determine the subsurface stresses under the combined normal and sliding contact on a elastic half space with a layer for different material properties of layers and substrate system. Cole and Sayles [10] developed a two dimensional numerical model for the contact of layered elastic bodies with real rough surfaces. They found that rough body layered contact has considerable influence on contact pressure behavior than smooth body layered contact. Also, Kuo and Keer [11] developed a three dimensional model to consider a multilayered half space under combined normal and sliding contact by a spherical indenter using Hankel transforms. They discussed the stress components for various coating thicknesses. Polonsky and Keer [12] applied the fast Fourier transform (FFT) technique with the multi-level multi-summation technique to the elastic layered contact problem. Chudoba et al. [13] developed a novel methodology based on the combination of theoretical image loads method and indentation experiments for the evaluation of the response of coated substrates to mechanical contact. They showed that the effects of the addition of intermediate layer to the coating/substrate systems. Although many researchers developed the

numerical models for the layered medium contact problems, their models were confined to the elastic contact behavior of the coating system.

As an alternative numerical approach, finite element analysis has been carried by a few researchers for the contact problem of layered surfaces. Komvopoulos [14] developed a two dimensional finite element model to investigate the thin layer effects on elastic semi-infinite solid compressed by a rigid body and found the general solutions for the subsurface stress and deformation fields. Also, the parametric analysis of layer thickness relative to Hertzian contact width size, friction coefficient and stiffness of layer were performed. Komvopoulos [15] extended the elastic layered media finite element model to the elastic-plastic contact problem of TiN/Ti coating system. The critical parameters such as layer thickness, material properties of layer and substrate materials and indentation depth on the threshold of plasticity of the elastic-plastic layered media indented by a rigid cylinder were examined. He found that the coating thickness plays an important role on the initiation and propagation of plastic zone and developed a deformation map for TiN/Ti coating systems. Bhattacharya and Nix [16] developed an elastic and plastic model to study the deformation associated with indentation of the thin film/substrate system using the finite element method and found the effects of the elastic and plastic properties of the materials on the hardness of the film/substrate system. Also the elastic compliance of the film/substrate system was determined as a function of the indentation depth from the load-displacement curve. Sun et al. [17] developed an elastic-plastic axisymmetric finite element model to investigate the effects of important parameters such as thickness of coatings and material properties of substrates on the various TiN coating/substrate systems. They found that substrate strength and layer thickness play significant roles on the load capacity of the systems, development of plastic zone, and subsequent coating failure. Kral and Komvopoulos [18] developed a three dimensional finite element model to determine the subsurface stress and strain fields due to sliding contact on an elastic-plastic layered medium. They found the effects of layer material properties, friction coefficient, and applied load on the stresses in the layer and the substrate. Ye and Komvopoulos [19] developed the three dimensional finite element model to investigate the effect of residual stress in the layered media due to normal and sliding loading and unloading conditions. They showed the optimum residual stress in the layer is a function of loading type and friction coefficient.



In the present study, a three dimensional finite element model has been developed to simulate the elastic plastic indentation process of the layered and gradient Ti/TiC coating system in order to determine the stress distribution and elastic-plastic deformation inside the multilayered and functionally gradient coating system. Also, a parametric study was performed to understand the effect of critical parameters on the stress distribution.

### 3.2 Description of the Layered and Gradient Ti/TiC Coating System

Interfaces between layers are prime locations for coating failure since considerably different mechanical properties between the layers exist. Therefore, multilayer coatings with gradually changing composition (functionally gradient) are highly desirable to avoid the drastic changes of mechanical properties. Figure 3.1 shows the typical layered and gradient Ti/TiC/DLC coating displaying the compositional variation of the Ti/TiC/DLC coating deposited on top of the 440C steel substrate [3]. Figure 3.2 depicts the indentation on the multilayered and gradient Ti/TiC coatings deposited on the semi-infinite medium with a rigid spherical indenter used for this study. Each coating surface is assumed to be smooth. The multilayered and gradient Ti/TiC coatings are assumed to be a series of perfectly bonded layers with unique material properties and layer thickness although the gradient coatings don't have distinct layers in reality, that is, they normally have continuous gradual change of Ti and C composition. The  $\alpha$ -Ti layer is deposited on the 440C stainless steel substrate as a bond layer in order to enhance the adhesion between the substrate and TiC coatings. Then coatings from  $\text{Ti}_{90}\text{C}_{10}$  to  $\text{Ti}_{30}\text{C}_{70}$  with variational Ti/C composition are continuously deposited on top of the bond layer. Figure 3.3 illustrates the schematic of functionally gradient (FG) Ti/TiC coating design used in this study. On top of the 440C stainless steel substrate,

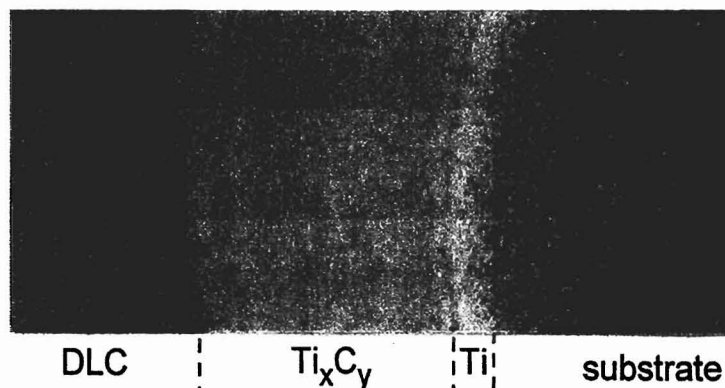


**Figure 3.1. Multilayered and functionally gradient Ti/TiC/DLC coating system that shows the gradual composition variation across the thicknesses of the layers.**

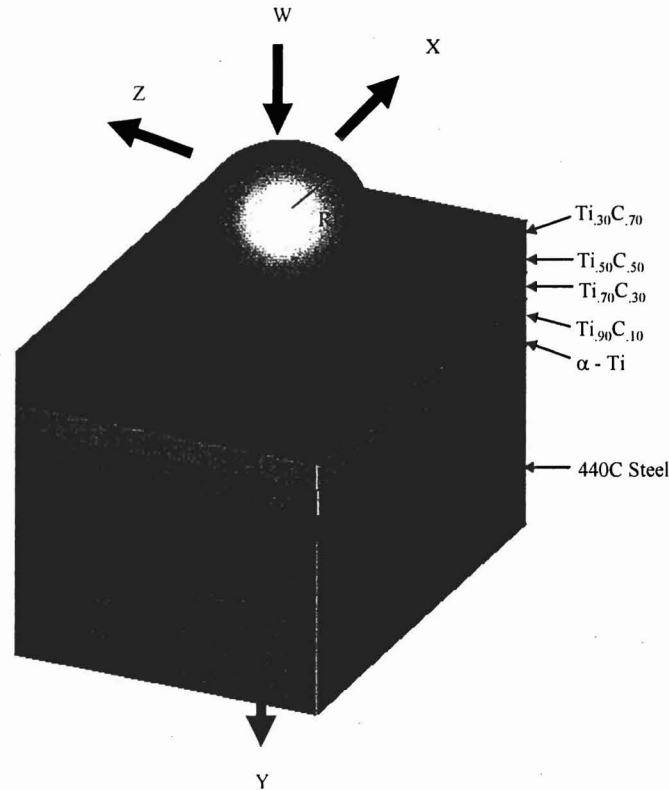


**Figure 3.2. Schematic of indentation with a rigid spherical indenter on multilayered semi-infinite medium.**

| Material                         | Hardness | Elastic Modulus | Thickness     | Poisson's Ratio |
|----------------------------------|----------|-----------------|---------------|-----------------|
| Ti <sub>30</sub> C <sub>70</sub> | 29 GPa   | 370 GPa         | 100 ~ 1000 nm | 0.20            |
| Ti <sub>50</sub> C <sub>50</sub> | 20 GPa   | 290 GPa         | 100 nm        | 0.20            |
| Ti <sub>70</sub> C <sub>30</sub> | 14 GPa   | 230 GPa         | 100 nm        | 0.25            |
| Ti <sub>90</sub> C <sub>10</sub> | 6 GPa    | 150 GPa         | 50 nm         | 0.25            |
| α-Ti                             | 4 GPa    | 140 GPa         | 50 nm         | 0.25            |
| 440C steel                       | 11 GPa   | 220 GPa         |               | 0.30            |

**Figure 3.3. Schematic of functionally gradient Ti/TiC coating design with compositional and mechanical properties variation.**

$\alpha$ -Ti is added as a bond layer with 50nm. On top of the  $\alpha$ -Ti layer, Ti<sub>90</sub>C<sub>10</sub> is deposited with 50 nm thickness. As the TiC composition changes, the gradient coating is generated. Each layer has its unique material properties such as hardness, elastic modulus, and Poisson's ratio.

Specific thickness for each layer is used for this application. Figure 3.3 consists of the material

property values used for the present study. The detail for TiC gradient coating procedure is well described in Voevodin et al. [3]. Table 3.1 contains the contact conditions such as normal loads, coefficients of friction, thicknesses of  $\text{Ti}_{.30}\text{C}_{.70}$  layer, indenter radius, and bond layers used in this analysis.

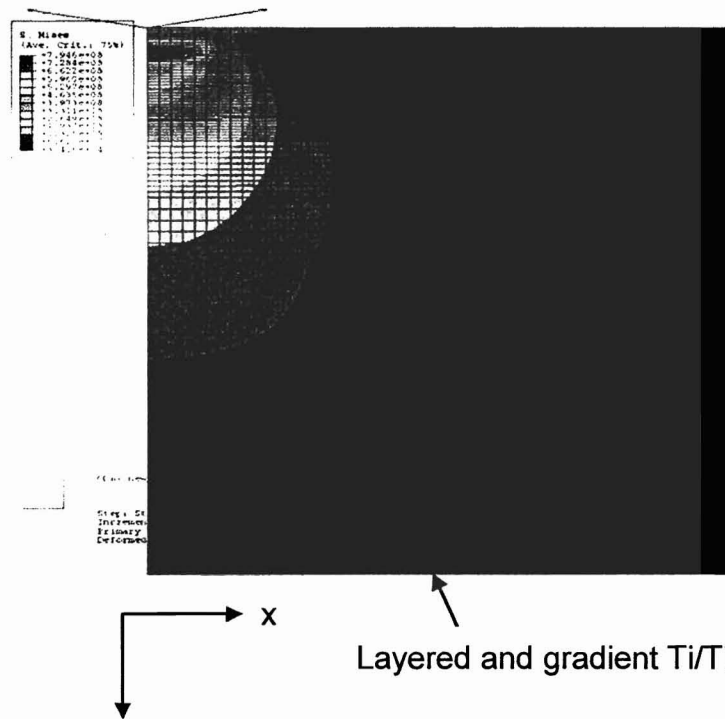
**Table 3.1. Contact conditions.**

|  |                                    |
|--|------------------------------------|
| Applied Normal Load (W)                          | $4.4 \times 10^{-4} \sim 0.15$ (N) |
| Coefficient of Friction ( $\mu$ )                | 0.0 ~ 0.6                          |
| Thickness of $\text{Ti}_{.30}\text{C}_{.70}$ (t) | 100 ~ 1000 (nm)                    |
| Radius of Indenter (R)                           | 0.0002 (m)                         |
| Bond Layers                                      | $\alpha$ -Ti, Ti Alloy, Chromium   |

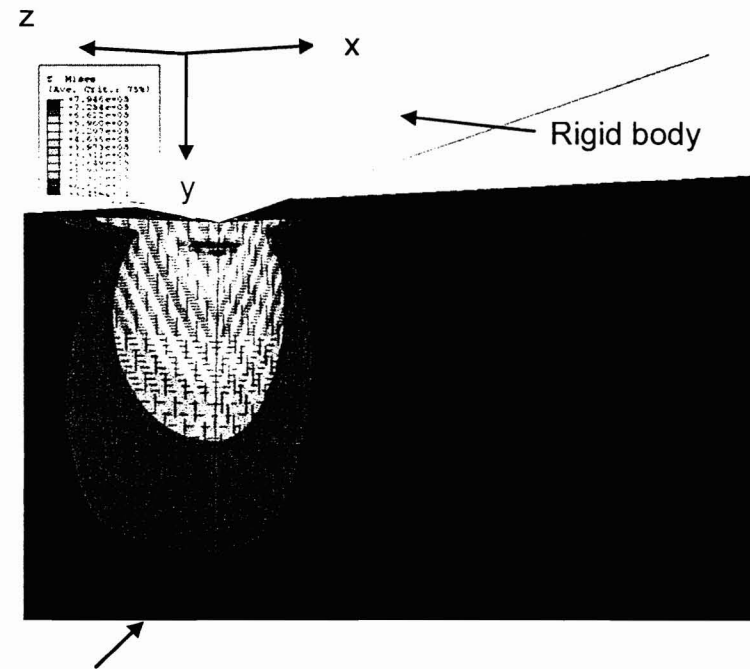
### 3.3 ABAQUS Finite Element Model

The contact problem described in Figure 3.2 can be modeled with the finite element mesh shown in Figure 3.4. The finite element model is to analyze contact stress distribution in layered and gradient Ti/TiC coating system generated by a rigid spherical indenter. The commercial finite element software package ABAQUS™/Standard was used to model the coating system under the plane-strain assumption. Due to the symmetry of the system, only a quarter of the computational domain was modeled. To reduce the computing time, the outer portion of computational domain was modeled as infinite body using infinite elements. In addition, very fine mesh was used for the gradient coatings adjacent to the coatings/rigid indenter interface near the contact zone in order to determine the stress distribution and deformation field accurately. Relatively coarse mesh was used for the region far away from the contact zone to reduce the computing time. Nearly 30,000 nodes and elements were used to model the entire system. Two types of elements, eight-node linear brick reduced integration element (C3D8R) and eight-node linear one-way infinite element (CIN3D8), were used for the coatings and semi-infinite medium. The coatings were modeled by assigning different material properties for the elements. The rigid spherical indenter is represented by a rigid spherical body with a radius of 0.2  $\mu\text{m}$ .

Coulomb friction was used to model the contact between the top coating surface and the rigid indenter. Due to the perfect bonding assumptions, the continuous displacement at the coating interfaces and coating/substrate interface is applied.



(a) -



(b)

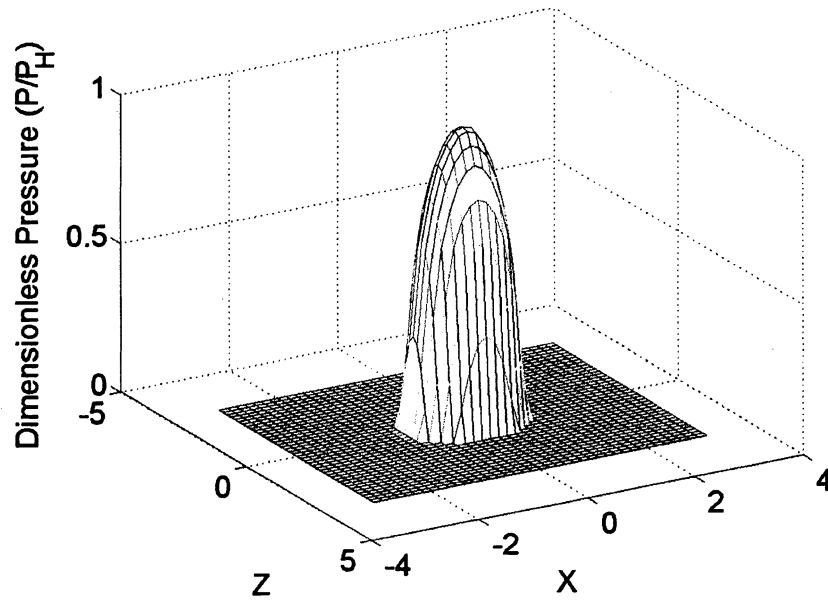
**Figure 3.4. Schematic of three dimensional finite element analysis model developed for the nanoindentation with a rigid spherical indenter tip on multilayered and functionally gradient coating system.**

Since the strain hardening is not considered, elastic perfectly plastic stress-strain relationships were used for the gradient coatings and the substrate. The onset of plastic yield begins by the von Mises yield criterion for the isotropic materials. Figure 3.4 illustrates the side and perspective view of the finite element model developed for this study. Figure 3.4 demonstrates the von Mises stress inside the coatings and substrate generated by a rigid spherical indenter on the plane of symmetry, x-y plane and x-y and y-z planes, respectively. The computation was performed using a workstation that consists of 9 dual-processor 900 MHZ Itanium2's with 2 Gigs of RAM each. Please note that the residual compressive stresses associated with the process of deposition are negligible because the layered and gradient coating thickness is a few micros.

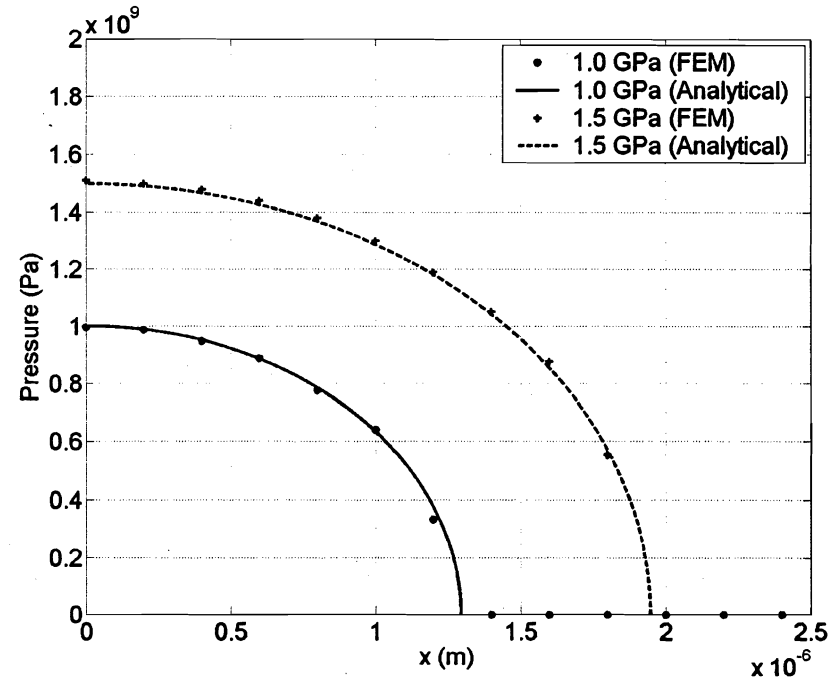
### **3.4 Results and Discussion**

In order to validate the three dimensional finite element model developed for this study, the elastic Hertzian point contact between the 440C stainless steel substrate and the rigid spherical indenter was performed. Figure 3.5 (a) shows the normalized Hertzian point contact pressure distribution generated by a rigid spherical indenter with the coefficient of friction,  $\mu = 0.0$ . Please note that the full contact pressure distribution was generated using the symmetry of the problem although a quarter of the computational domain was modeled. The magnitude of maximum Hertzian pressure is 1.0 GPa under a normal load,  $W = 0.0035$  N. Figure 3.5 (b) depicts the contact pressure distributions at the center of the contact along the axis of symmetry obtained by finite element and analytical solutions for maximum Hertzian contact pressure, 1.0 GPa and 1.5 GPa, respectively. The slight discrepancy between the finite element and analytical results at the contact edge is due to the node discretization size of the contact elements. The results indicate that there is good agreement between the finite element and analytical solutions.

The full von Mises stress distribution on the plane of symmetry was plotted using the symmetry of the problem. Von Mises stress is taken into account to analyze and predict the failure in the contact problems. Figure 3.6 represents the von Mises stress distributions generated by a rigid spherical indenter inside the 440C stainless steel substrate on the vertical plane of symmetry, i.e., X-Y plane for a normal load

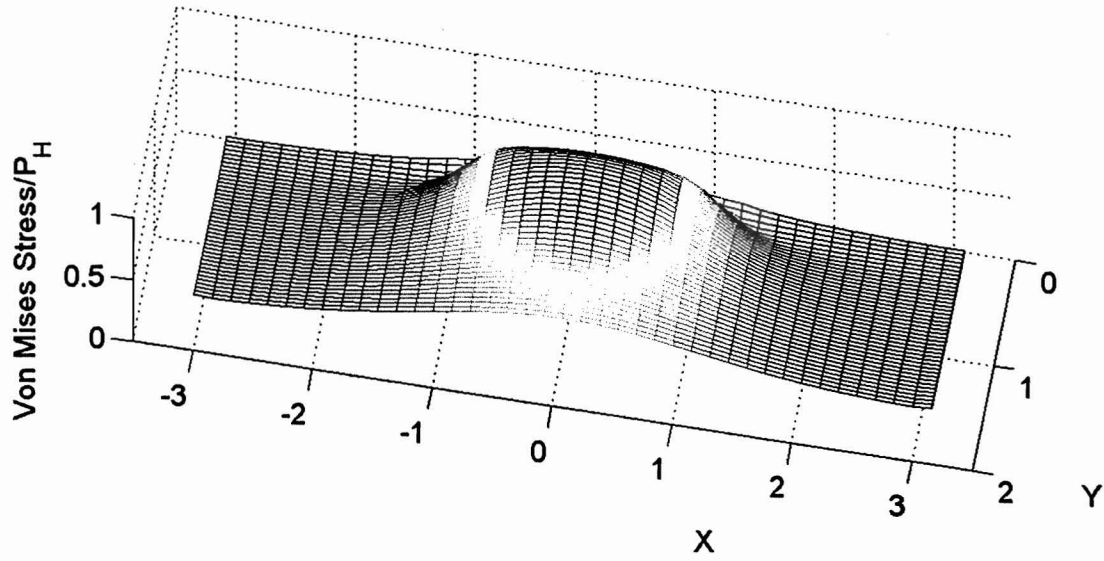


(a)

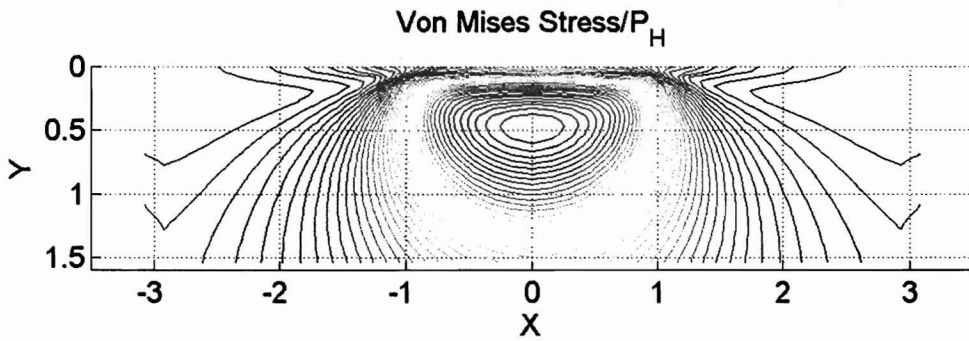


(b)

**Figure 3.5. Hertzian contact pressure distribution on semi-infinite medium indented by a rigid spherical indenter; (a) normalized contact pressure distribution by finite element solution for  $W = 0.0035$  N and (b) contact pressure distributions at the center of contact along the plane of symmetry obtained by finite element and analytical solutions.**



(a)



(b)

**Figure 3.6. Von Mises stress distribution in semi-infinite medium indented by a rigid spherical indenter for normal load,  $W = 0.0035 \text{ N}$  ( $\mu = 0.0$ ); (a) perspective view of normalized von Mises stress on the plane of symmetry and (b) contour plot of normalized von Mises stress on the plane of symmetry.**

$W = 0.0035 \text{ N}$  and  $\mu = 0.0$ . Figure 3.6(a) depicts the perspective view of normalized von Mises stress at the center of the contact on the vertical plane of symmetry. This figure displays the smooth variation of von Mises stress along the depth direction,  $Y$ , as well as along the surface direction,  $X$ . The calculated maximum von Mises stress is  $0.635 P_h$  located approximately at  $Y = 0.5$  below the surface. Figure 3.6(b) illustrates the contour of the von Mises stress distribution presented in Figure 3.6(a).

Figure 3.7 demonstrates stress component profile variations below the surface at the center of the contact along the axis of depth for  $W = 0.0035$  N and  $\mu = 0.0$ . Various lines are generated by the finite element solutions. Dots are generated by the analytical solutions for the same contact conditions.  $\sigma_x$  decreases rapidly as the depth increases. Due to the symmetry,  $\sigma_z$  has the same values with  $\sigma_x$  along the depth direction.  $\sigma_y$  has the maximum value, 1, at the surface and decreases gradually as the depth increases.  $\sigma_{mises}$  has the maximum value of  $0.635 P_h$  located approximately at  $Y = 0.5$  on the depth axis. In general, the good agreement for stress distribution between the finite element and analytical solutions was achieved at the various depths below the contact surface.

Figure 3.8 shows the stress component profile variations below the surface at the center of the contact along the axis of depth for  $W = 0.0035$  N and  $\mu = 0.0$ . The stress components such as  $\sigma_x$ ,  $\sigma_y$ ,  $\sigma_z$ , and  $\sigma_{mises}$  are displayed. The diagram depicts the layered and gradient Ti/TiC coating system with 350 nm  $Ti_{.30}C_{.70}$  layer thickness. The stress component profiles display the discontinuities occurring at the interfaces due to the material property differences.

Fundamentally, the layers behave as beams bonded to the substrate. The maximum von Mises stress occurs at the  $Ti_{.50}C_{.50}$  and  $Ti_{.70}C_{.30}$  interface. The von Mises stress difference at the interfaces is not exceeding 0.1 GPa.  $\sigma_x$  and  $\sigma_z$  is more influenced by the layered and gradient coatings while  $\sigma_y$  is less influenced. The magnitude and location of maximum von Mises stress can be altered significantly when the different design of layered and gradient coating system is used.

Figure 3.9 represents the von Mises stress distribution in the layered and gradient Ti/TiC coating system on the plane of symmetry for the normal loading contact conditions with 350nm  $Ti_{.30}C_{.70}$  layer thickness,  $W = 0.0035$  N and  $\mu = 0.0$ . Figure 3.9(a) shows the perspective view of the von Mises stress generated by a rigid spherical indenter



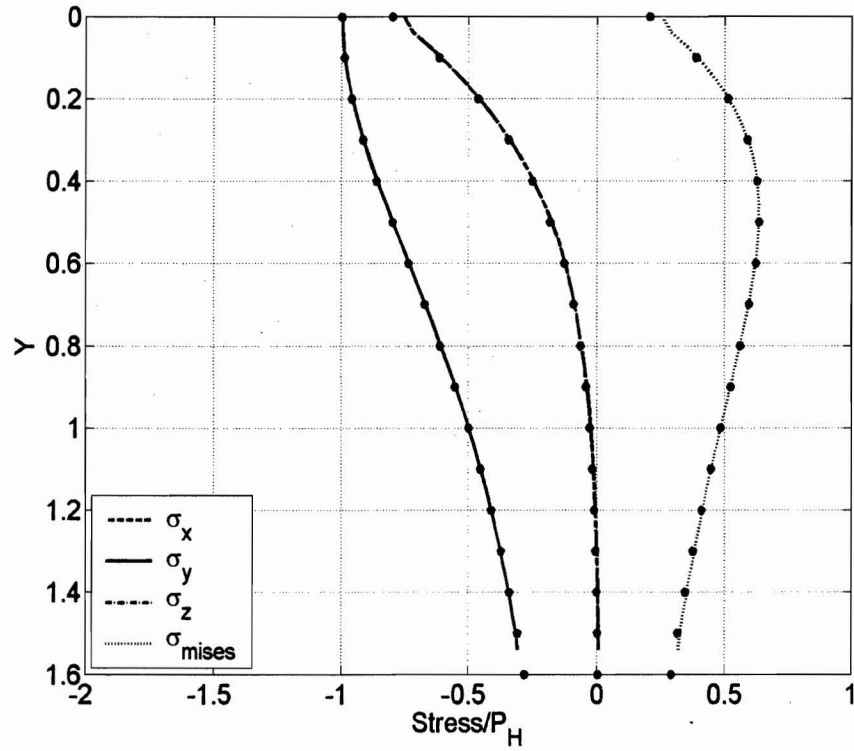


Figure 3.7. Analytical and finite element solutions of normalized stresses in the semi infinite medium due to the normal load at the surface ( $\mu = 0$ ).

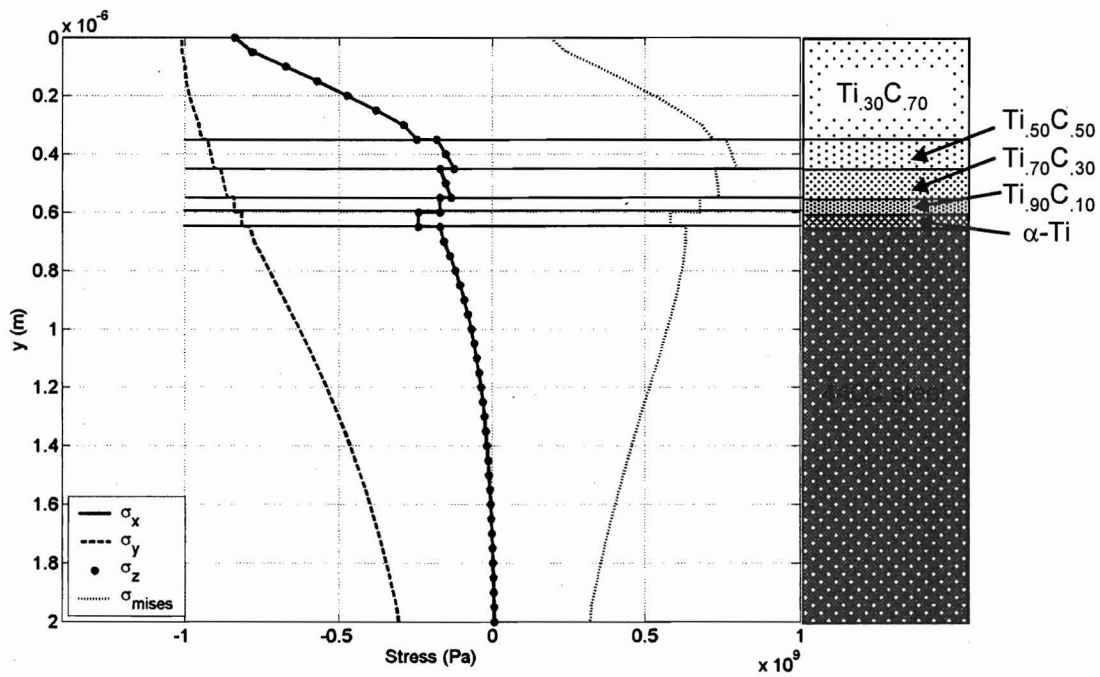
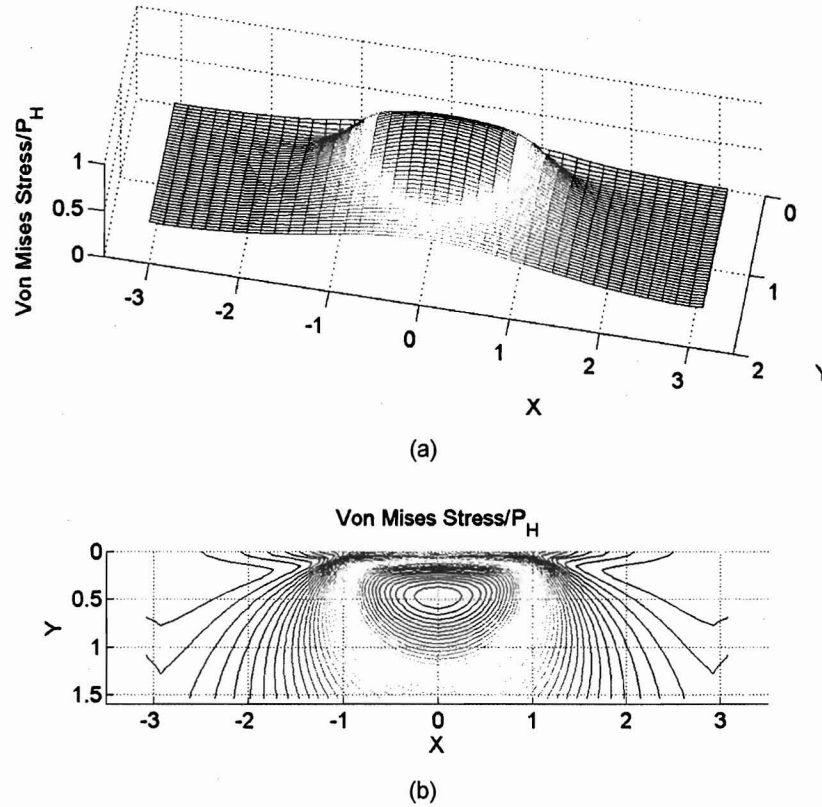


Figure 3.8. Analytical and finite element solutions of the stresses in a layered and gradient coating system due to normal load at the surface ( $\mu = 0.0$ ).



**Figure 3.9. Von Mises stress distribution in layered and gradient Ti/TiC coating system indented by a rigid spherical indenter for indentation load,  $W = 0.0035 \text{ N}$  ( $\mu = 0.0$ ); (a) perspective view of normalized von Mises stress on the plane of symmetry and (b) contour plot of normalized von Mises stress on the plane of symmetry.**

on the plane of symmetry. Instead of having smooth von Mises stress distribution inside the layered and gradient Ti/TiC coatings, discontinuous stress distribution at the layered and gradient coating interfaces exists due to the material property differences. Overall shape of von Mises stress distribution is similar to the one without the layered and gradient Ti/TiC coating. The calculated maximum von Mises stress is 795 MPa located at  $\text{Ti}_{.50}\text{C}_{.50}$  and  $\text{Ti}_{.70}\text{C}_{.30}$  interface along the depth direction below the surface. Figure 3.9(b) demonstrates the contour of the von Mises stress distribution presented in Figure 3.9(a).

Figure 3.10 shows the effect of coating design on von Mises stress for the normal load,  $W = 0.0035 \text{ N}$  and  $\mu = 0.0$ . Figure 3.10 illustrates the von Mises stress distribution comparison between a 700 nm  $\text{Ti}_{.30}\text{C}_{.70}$  layer coating on 440C steel substrate and a 700 nm layered and gradient Ti/TiC coating on 440C steel substrate. Please note that the von Mises stress distributions are obtained at the center of the contact along the axis of depth below the contact surface. The magnitude of von Mises stresses occurred inside the  $\text{Ti}_{.70}\text{C}_{.30}$ ,  $\text{Ti}_{.90}\text{C}_{.10}$  and  $\alpha\text{-Ti}$

coatings are smaller than the one of the monolayer coating because of the low moduli of elasticity for  $\text{Ti}_{.70}\text{C}_{.30}$ ,  $\text{Ti}_{.90}\text{C}_{.10}$  and  $\alpha\text{-Ti}$  coatings. Monolayer coating depicts the sharp von Mises stress discontinuity occurring at the interface due to the high modulus difference of film and substrate. However, the layered and gradient  $\text{Ti}/\text{TiC}$  coating represents the gradual stepped von Mises stress changes. While the monolayer coating has the maximum von Mises stress at the  $\text{Ti}_{.30}\text{C}_{.70}$  and substrate interface, the layered and gradient  $\text{Ti}/\text{TiC}$  coating has its maximum von Mises stress at the  $\text{Ti}_{.50}\text{C}_{.50}/\text{Ti}_{.70}\text{C}_{.30}$  interface. The magnitude of maximum von Mises stress decreases from 0.909 GPa to 0.818 GPa when the monolayer coating is replaced by the layered and gradient  $\text{Ti}/\text{TiC}$  coating. Therefore, the layered and gradient coating is more beneficial than monolayer coating since it reduces the magnitude of maximum von Mises stress in the coating system. In addition, it results in lower magnitude differences of von Mises stress at the interfaces.

In order to represent the spatial distribution of von Mises stress in the layered and gradient  $\text{Ti}/\text{TiC}$  coating system, the results from the FEA model are presented. Figure 3.11 shows contours of von Mises stress in the layered and gradient  $\text{Ti}/\text{TiC}$  coating system indented by a rigid spherical indenter on the plane of symmetry, X - Y plane.

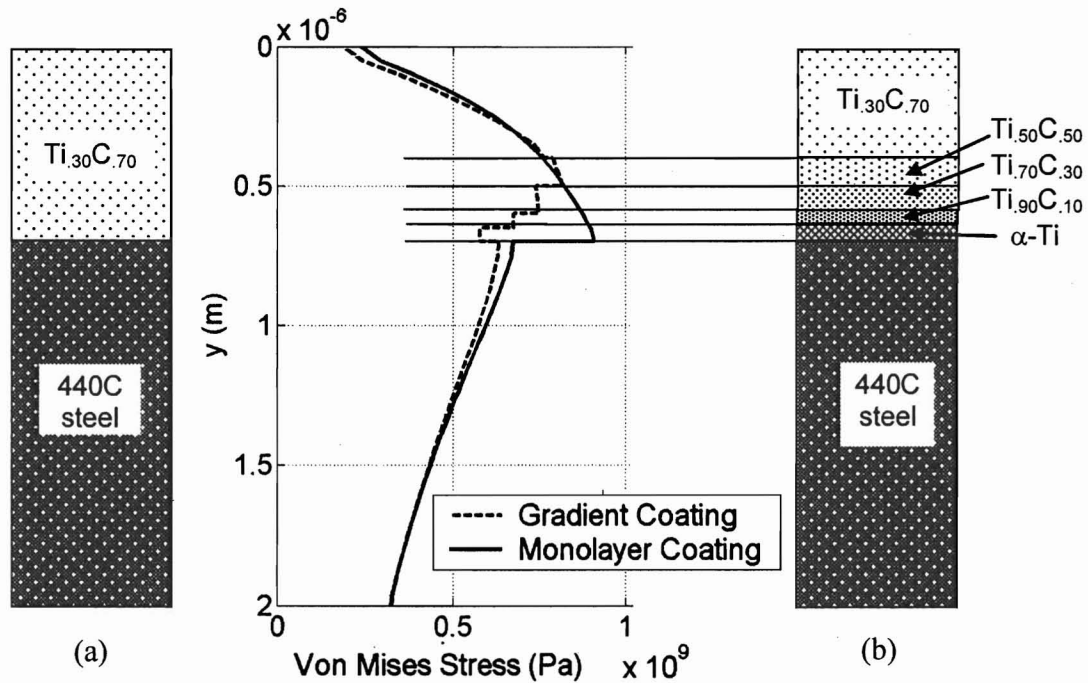
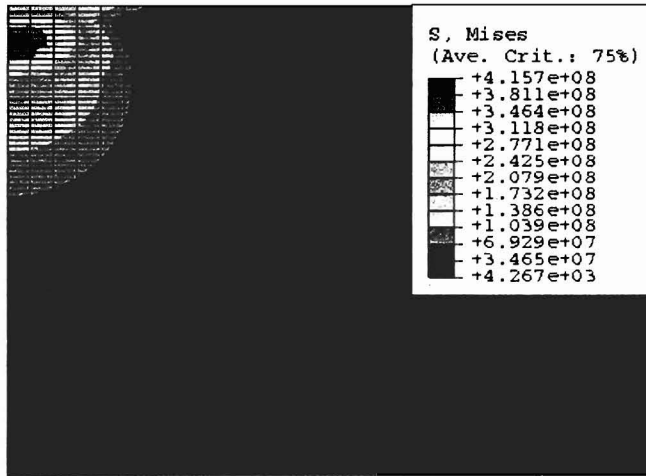
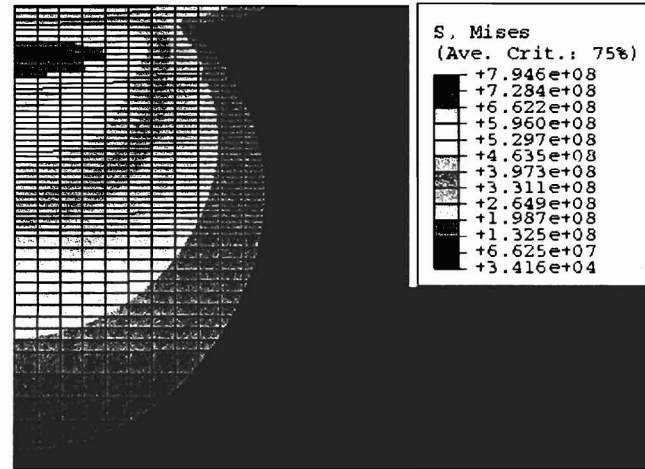


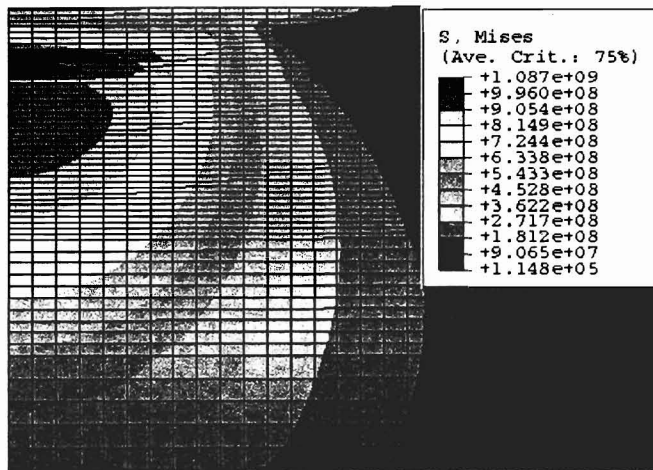
**Figure 3.10. Effect of coating design on von Mises stress in (a) monolayer coating system and (b) layered and gradient coating system for normal load,  $W = 0.0035 \text{ N}$  ( $\mu = 0.0$ ).**



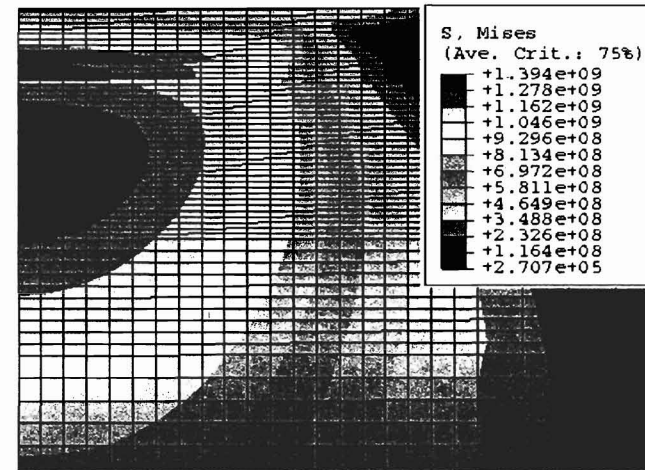
(a)



(b)



(c)

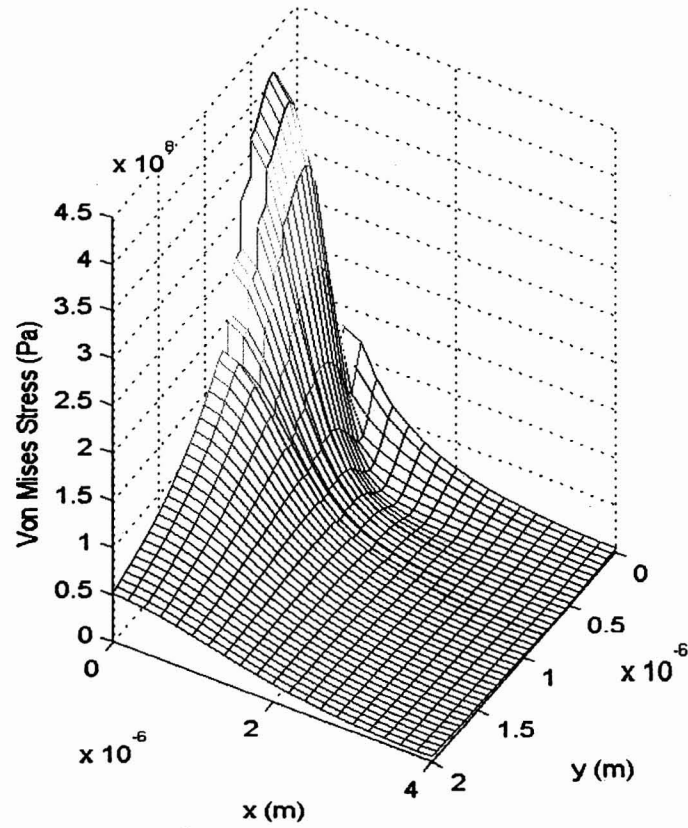


(d)

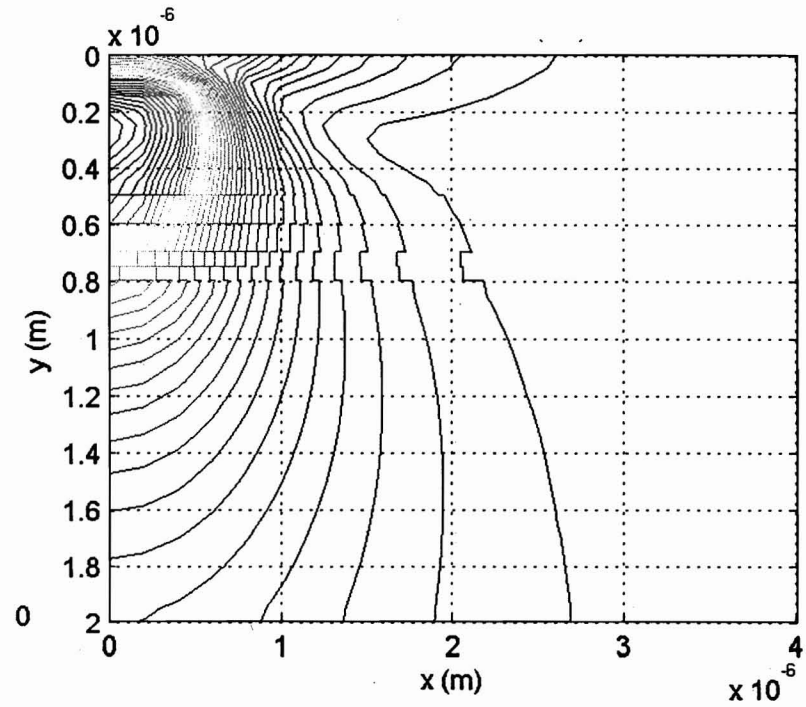
**Figure 3.11. Contour plots of von Mises stress in layered and gradient coating system indented by a rigid spherical indenter for normal load; (a)  $W = 4.4 \times 10^{-4}$  N, (b) 0.0035 N, (c) 0.0119 N, and (d) 0.0283 N.**

Figure 3.11 illustrates that the von Mises stress fields below the surface vary as the load increase from  $W = 4.4 \times 10^{-4}$  N through 0.0283 N with  $\mu = 0.0$ . Please note that the maximum von Mises stress always occurs at certain depth along the axis of depth below the center of the contact due to the symmetry of the problem. Figure 3.11(a) is the contour plot of von Mises stress for a normal load,  $W = 4.4 \times 10^{-4}$  N. The maximum von Mises stress occurs inside the  $\text{Ti}_{.30}\text{C}_{.70}$  coating with the magnitude of 415.7 MPa. With the relatively light normal load,  $W = 4.4 \times 10^{-4}$  N, only shallow indentation depth occurs and shows the elastic behavior of the coating/substrate system. Figure 3.11(b) is the contour plot of von Mises stress for a normal load,  $W = 0.0035$  N. The maximum von Mises stress occurs inside the  $\text{Ti}_{.50}\text{C}_{.50}$  coating with the magnitude of 794.6 MPa. Figure 3.11(c) is the contour plot of von Mises stress for a normal load,  $W = 0.0119$  N. The maximum von Mises stress occurs inside the  $\text{Ti}_{.50}\text{C}_{.50}$  coating with the magnitude of 1.087 GPa. Figure 3.11(d) is the contour plot of von Mises stress for a normal load,  $W = 0.0283$  N. The maximum von Mises stress occurs inside the substrate with the magnitude of 1.394 GPa. In general, as the applied normal load increases, the location of maximum von Mises stress moves from inside the layered and gradient Ti/TiC coatings to substrate. Also, as load increases, wider half Hertzian contact width and higher von Mises stress are generated. Due to the material discontinuities inside the layered and gradient Ti/TiC coatings, there is discontinuous stress distribution at the interfaces below the contact surface.

Figure 3.12 depicts the von Mises stress distribution on the plane of symmetry, X-Y plane, for 500nm  $\text{Ti}_{.30}\text{C}_{.70}$  layer thickness,  $W = 4.4 \times 10^{-4}$  N and  $\mu = 0.0$ . Figure 3.12(a) is the perspective view of the von Mises stress distribution generated below the contact surface along the axis of depth. It illustrates that the maximum von Mises stress with the magnitude of 0.408 GPa occurring inside the top  $\text{Ti}_{.30}\text{C}_{.70}$  coating. Due to the discontinuous material properties at the coating interface, von Mises stress distribution displays drastic stress variations at the interface along the axis of depth. Figure 3.12(b) is the contour plot of von Mises stress distribution presented in Figure 3.12(a). Figure 3.13 shows the effect of top  $\text{Ti}_{.30}\text{C}_{.70}$  coating thickness on von Mises stress for  $W = 0.0035$  N and  $\mu = 0.0$ . Depending on the top  $\text{Ti}_{.30}\text{C}_{.70}$  coating thickness, the stress distributions along the axis of depth at the center of the contact vary significantly. With 100nm top  $\text{Ti}_{.30}\text{C}_{.70}$  coating thickness, the maximum von Mises stress, 628 MPa, occurs at the  $\text{Ti}_{.90}\text{C}_{.10}$  and  $\alpha$  - Ti interface. As the top coating thickness increases to



(a)



(b)

**Figure 3.12. Von Mises stress distribution in layered and gradient coating system indented by a rigid spherical indenter for  $\text{Ti}_{30}\text{C}_{70}$  coating thickness, 500nm, normal load,  $4.4 \times 10^{-4}$  N, and friction coefficient, 0.0; (a) von Mises stress distribution and (b) contour plot of von Mises stress.**

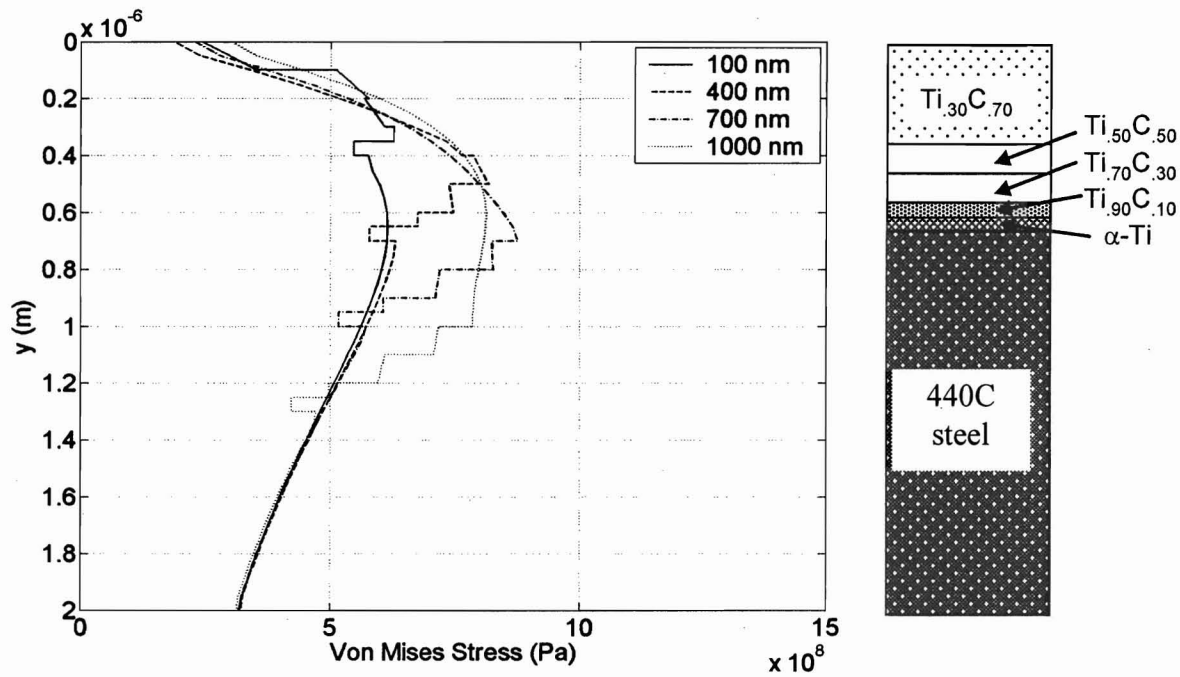


**Figure 3.13. Effect of top  $\text{Ti}_{30}\text{C}_{70}$  coating thickness on von Mises stress in layered and gradient coating system for various  $\text{Ti}_{30}\text{C}_{70}$  thicknesses ( $W = 0.0035$  and  $\mu = 0.0$ ).**

400nm, the location of maximum von Mises stress, 818 MPa, moves to the  $\text{Ti}_{50}\text{C}_{50}$  and  $\text{Ti}_{70}\text{C}_{30}$  interface. When the top coating thickness is 700 nm, the maximum von Mises stress, 875 MPa, occurs at the  $\text{Ti}_{30}\text{C}_{70}$  and  $\text{Ti}_{50}\text{C}_{50}$  interface. Finally, when the 1000 nm thickness is used, the maximum von Mises stress, 813 MPa, occurs inside the top  $\text{Ti}_{30}\text{C}_{70}$  coating. The thicker  $\text{Ti}_{30}\text{C}_{70}$  coating (1000 nm) results in less magnitude of maximum von Mises stress than intermediate coatings thicknesses (400 nm and 700 nm). The results indicate that the maximum von Mises stress location can be moved vertically along the axis of depth depending on the coating thickness under the same normal load while the von Mises stress in the substrate changes negligibly. Also, the results suggest that the desirable top coating thickness changes depending on the loading conditions. Therefore the top layer thickness has a significant effect on the magnitude of the von Mises stress developed in the layered and gradient Ti/TiC coating system. It is noted that the maximum thickness of the top  $\text{Ti}_{30}\text{C}_{70}$  layer is affected by the residual compressive stresses due to the thermal expansion coefficient differences.

Figure 3.14 depicts the effect of top coating thickness on contact pressure distribution indented by a rigid spherical indenter on the contact surface under  $W = 0.0035$  N and  $\mu = 0.0$ . The dashed line represents the pressure distribution generated on the semi-infinite medium without coatings. It illustrates the maximum Hertzian pressure, 1.0 GPa, is generated under the

normal load,  $W = 0.0035$  N. When the layered and gradient Ti/TiC coating system is applied, the maximum Hertzian pressure increases due to the stiffer coating layers. The dashdot line pressure distribution is generated for the 500nm top  $\text{Ti}_{.30}\text{C}_{.70}$  layer thickness of layered and gradient Ti/TiC coating system. Due to the stiffer material properties of the coatings, the magnitude of maximum Hertzian pressure is higher with the narrower half contact width compared with the no layer Hertzian contact condition. The solid line pressure distribution is generated for the 1000nm top  $\text{Ti}_{.30}\text{C}_{.70}$  layer thickness of layered and gradient Ti/TiC coating system. This line demonstrates highest magnitude of von Mises stress with the narrowest half contact width under the normal load,  $W = 0.0035$  N. In general, the pressure magnitude increases due to not only the increase of Young's modulus but also the increase of top  $\text{Ti}_{.30}\text{C}_{.70}$  coating thickness although the same normal load,  $W = 0.0035$  N, is applied. In addition, the half Hertzian contact width decreases as the top coating thickness increases because the same magnitude of normal load is applied to the layered and gradient Ti/TiC coating system.

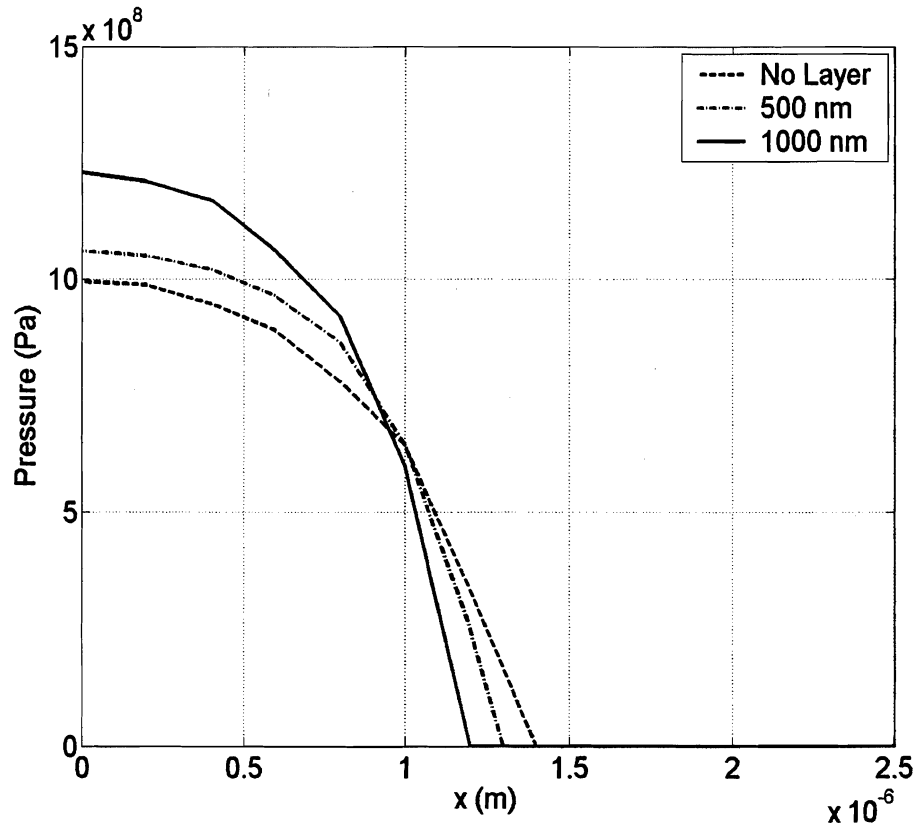


**Figure 3.14. Effect of top coating thickness on contact pressure distribution on layered and gradient coating system indented by a rigid spherical indenter (  $W = 0.0035$  N,  $\mu = 0.0$  ).**



Figure 3.15 shows the effects of applied load on von Mises stress in layered and gradient Ti/TiC coating system indented by a rigid spherical indenter for various normal loads with 350nm Ti<sub>30</sub>C<sub>70</sub> layer thickness and  $\mu = 0.0$ . The magnitude of von Mises stress in the layered and gradient Ti/TiC coating system increases as the applied normal load increases from 0.0004N to 0.0283 N. The maximum von Mises stress for the normal load,  $W = 0.0004\text{N}$ , is 416 MPa occurring at the Ti<sub>30</sub>C<sub>70</sub> and Ti<sub>50</sub>C<sub>50</sub> interface. As the normal load increases, the magnitude and location of the maximum von Mises stress are changed. The maximum von Mises stress for the normal load,  $W = 0.0035\text{ N}$ , is 795 MPa occurring at the Ti<sub>50</sub>C<sub>50</sub> and Ti<sub>70</sub>C<sub>30</sub> interface. The maximum von Mises stress for the normal load,  $W = 0.0119\text{ N}$ , is 1.09 GPa at the Ti<sub>50</sub>C<sub>50</sub> and Ti<sub>70</sub>C<sub>30</sub> interface. Finally the maximum von Mises stress for the normal load,  $W = 0.0283\text{ N}$ , is 1.39 GPa at the Ti<sub>50</sub>C<sub>50</sub> and Ti<sub>70</sub>C<sub>30</sub> interface. Generally the magnitude and location of maximum von Mises stress distribution vary significantly depending on the magnitude of normal load when the layered and gradient Ti/TiC coating system is used.

Figure 3.16 depicts the effect of bond layer material on von Mises stress for  $W = 0.0035\text{ N}$  and  $\mu = 0.0$ . Bond layer materials such as  $\alpha$ -Ti, Ti alloy, and chromium are used. Table 3.2 contains the material properties such as modulus of elasticity and Poisson's ratio for three bond layers. There are significant von Mises stress changes inside the bond layer. The higher the modulus of elasticity is, the higher the von Mises stress is. The negligible von Mises stress changes occur in the other coatings and substrate even if the substantial von Mises stress variation occurs in the bond layer. Using the stiffer bond layer like chromium increases the resistance to initiation of plastic deformation in the bond layer. However, it creates the higher von Mises stress differences at the interfaces above and below the bond layer.

**Table 3.2. Material properties for bond layers.**

|               | Modulus of Elasticity (GPa) | Poisson's Ratio |
|---------------|-----------------------------|-----------------|
| $\alpha$ - Ti | 140                         | 0.25            |
| Ti Alloy      | 103                         | 0.34            |
| Chromium      | 279                         | 0.21            |

In order to investigate the friction effect at the contact interface, the Coulomb friction was used at the rigid indenter and Ti<sub>30</sub>C<sub>70</sub> coating interface. Figures 3.17 demonstrates the von Mises stress distribution generated in 350 nm Ti<sub>30</sub>C<sub>70</sub> layer thickness coating system at the center of the contact along the axis of depth under the normal loading conditions for  $W = 4.4 \times 10^{-4}\text{ N}$  and  $W = 0.0283\text{ N}$ . Figure 3.17(a) illustrates that the effect of friction coefficient

variation from  $\mu = 0.0$  to  $\mu = 0.3$  on von Mises stress variation near the surface is negligible under the low loading condition. The maximum von Mises stresses are produced at the  $Ti_{.30}C_{.70}$  and  $Ti_{.50}C_{.50}$  interface for  $\mu = 0.0$  through 0.3. At higher loading,  $W = 0.0283$  N, there are significant von Mises stress distribution changes near the contact because the friction (tangential) force at the contact is proportional to applied load shown in Figure 3.17(b).

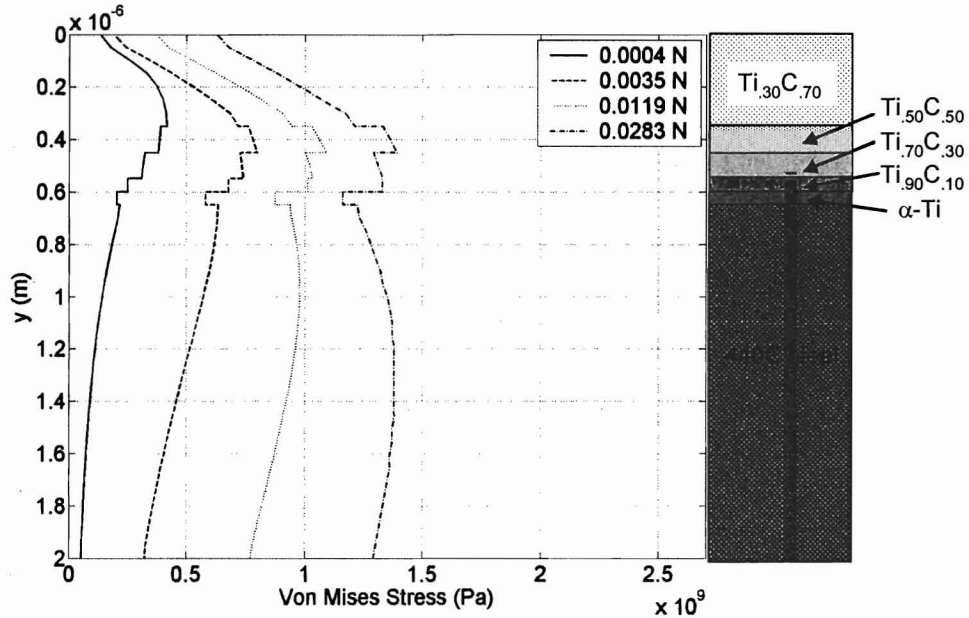


**Figure 3.15. Effect of applied load on von Mises stress in layered and gradient coating system indented by a rigid spherical indenter for various normal loads ( $Ti_{.30}C_{.70} = 350$  nm,  $\mu = 0.0$ ).**

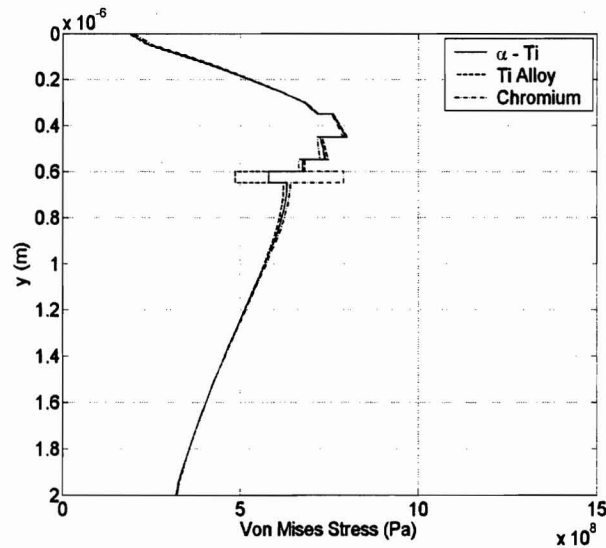
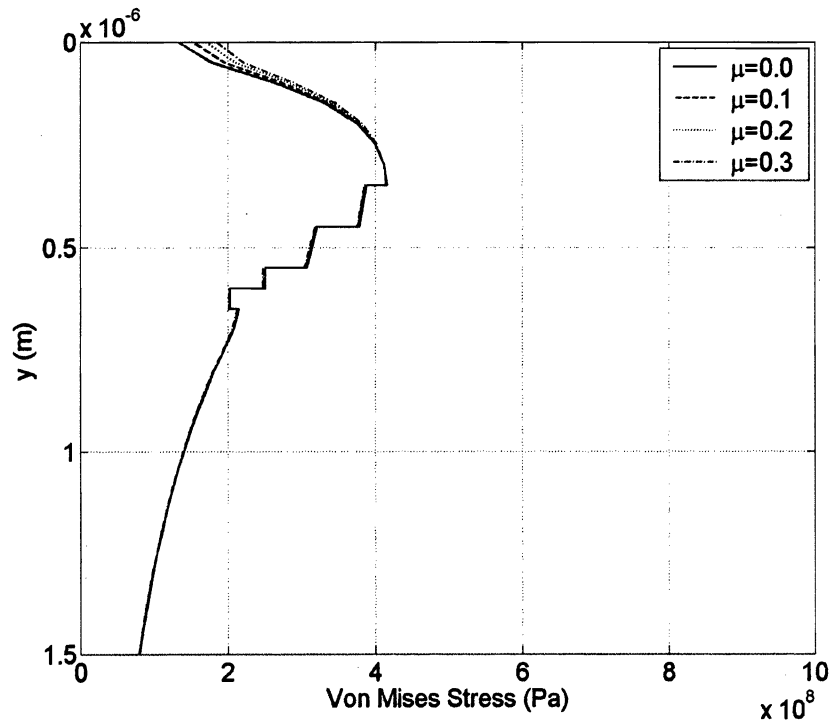
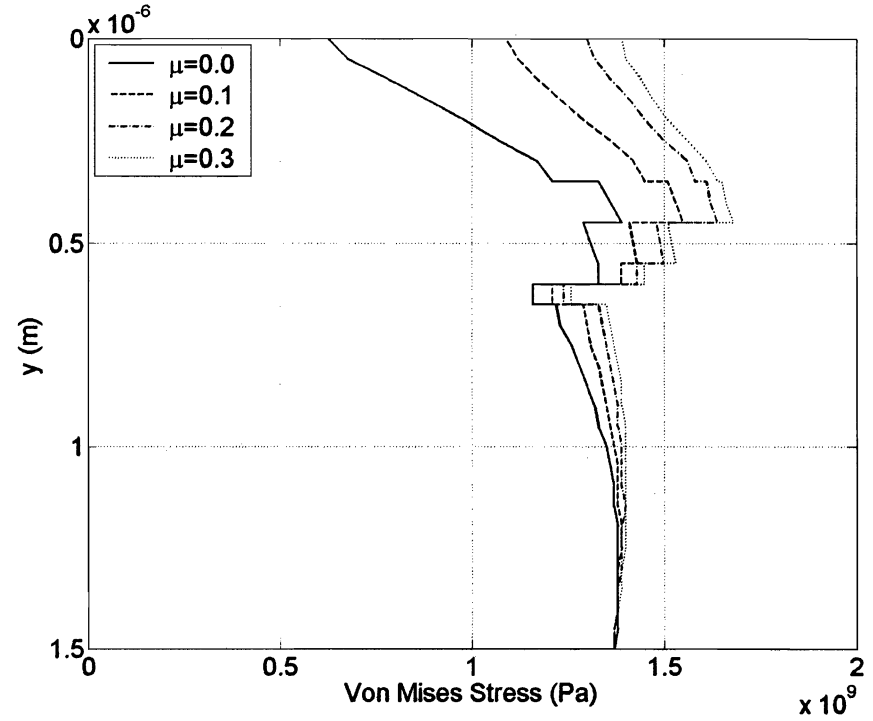


**Figure 3.16. Effect of bond layer materials on von Mises stress in layered and gradient coating system for  $W = 0.0035$  N and  $\mu = 0.0$ .**



(a)



(b)

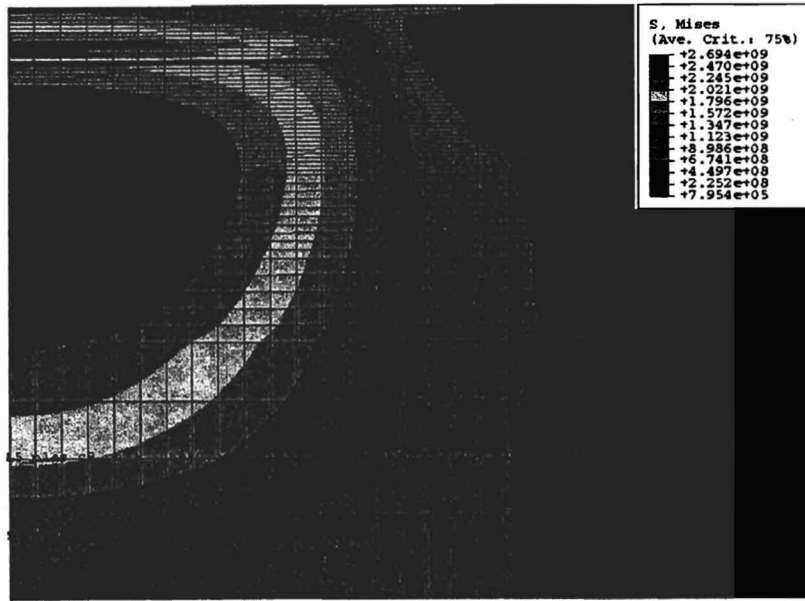
**Figure 3.17. Effect of friction coefficient on von Mises stress in layered and gradient coating system for normal load (a)  $W = 4.4 \times 10^{-4}$  N and (b)  $W = 0.0283$  ( $\text{Ti}_{.30}\text{C}_{.70} = 350$  nm).**

Also, the magnitude of maximum von Mises stress increases as the friction coefficients increase. However, the location of von Mises stress remains the same, at the  $\text{Ti}_{.50}\text{C}_{.50}$  and  $\text{Ti}_{.70}\text{C}_{.30}$  interface.

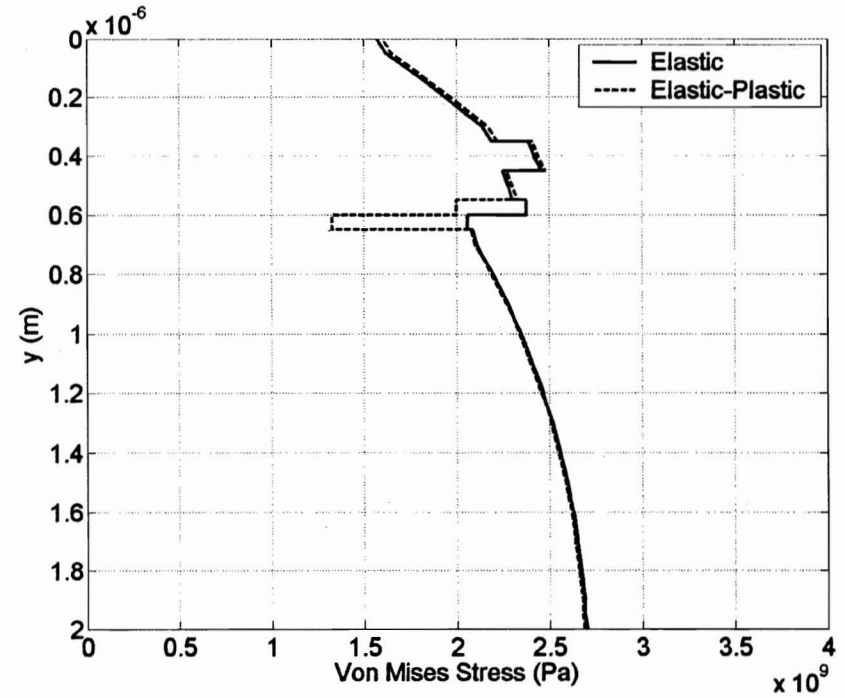
Figure 3.18 shows the effect of plasticity on von Mises stress for 350 nm  $\text{Ti}_{.30}\text{C}_{.70}$  layer thickness,  $W = 0.15$  N and  $\mu = 0.0$ . In order to obtain the yield strength of the materials used for the coating system, the following relationship is used because the strain-hardening is negligible for the coating materials used (Komvopolous, [15]).

$$\sigma_{yield} = \frac{\text{hardness}}{3}$$

Linear elastic-perfectly plastic stress-strain law was applied for the FEA model. Figure 3.18(a) demonstrates that the contour plot of von Mises stress indented by a rigid spherical indenter at the center of the contact. It depicts the high stress concentration inside the  $\text{Ti}_{.50}\text{C}_{.50}$  layer. Also, it shows that the maximum von Mises stress occurs inside the substrate. Figure 3.18(b) illustrates von Mises stress at the center of contact along the axis of depth. Significant plastic deformation is developed inside the  $\text{Ti}_{.30}\text{C}_{.70}$  and  $\alpha\text{-Ti}$  coatings because the yield strength of the materials was reached as the normal load increases. Therefore, the plastic deformation of the coatings is initiated at the bond layer interface. Plastic deformation is the major concern in design of the layered and gradient coating/substrate system because the tribological coating failure usually initiates and propagates from the plastic deformation zone.



(a)



(b)

**Figure 3.18. Effect of plasticity on von Mises stress in layered and gradient coating system for  $\text{Ti}_{.30}\text{C}_{.70} = 350 \text{ nm}$ ,  $W = 0.15 \text{ N}$ , and  $\mu = 0.0$ ; (a) contour plot of von Mises stress on the plane of symmetry and (b) stress profile of von Mises stress along the centerline of the contact for elastic material properties and elastic-plastic material properties.**

### **3.5 Summary and Conclusion**

Stress distributions in a layered and gradient TiC coating/440C steel substrate system indented by a rigid spherical indenter were determined using the finite element analysis model. Design superiority of the layered and gradient coating to monolayer coating was proved to improve the integrity of coating system. The layered and gradient Ti/TiC coatings generate smooth discrete stress transition at the coating interfaces when the chemistry and structure of the coating is varied. Therefore, the stress discontinuities at the interfaces are important design factor to consider. Top layer thickness is very influential to the layered and gradient Ti/TiC coating system because it changes the magnitude and location of maximum von Mises stress distribution inside the coating system significantly. Also, the top layer thickness changes the magnitude of maximum Hertzian pressure and half contact width under the same load condition due to the combination of the stiffness and thickness of the layer material. In addition, magnitude of the applied normal load affects the maximum Hertzian contact pressure and subsurface von Mises stress significantly. Effect of friction on subsurface von Mises stress is small for low loading conditions. However, effect of friction on subsurface von Mises stress is substantial for high loading conditions. Effect of the bond layer materials on the von Mises stress should be considered because yielding in the layered and gradient Ti/TiC coating system initiates at the bond layer when  $\alpha$ -Ti bond layer is used.

In conclusion, stress distribution in the layered and gradient Ti/TiC coating system indented by a rigid spherical indenter depends strongly on many critical parameters such as the layer thicknesses, coating design, material properties, applied load, and the friction. Especially, the magnitude, location, and discontinuity of the von Mises stress at the interfaces play important roles on the interfacial failure of the coating system. Design of coating systems with layered and gradient Ti/TiC coatings increases the limitation of their applications when the loading conditions are specified.

## **4.0 NANOINDENTATION AND FINITE ELEMENT ANALYSIS OF MULTILAYERED AND FUNCTIONALLY GRADIENT TRIBOLOGICAL COATINGS**

### **4.1 Introduction**

Nanoindentation has become widely used for the characterization of coated systems over the past three decades. Doerner and Nix [20] developed a method for interpreting hardness and Young's modulus from the data obtained from depth-sensing indentation instruments. Later,

Pharr and Oliver [21] proposed the improved nanoindentation technique and conducted the experimental measurements of thin film mechanical properties such as hardness and modulus of elasticity, that is, properties are derived from measurements of load, displacement, and time. Page and Hainsworth [22] reviewed and summarized the abilities and limitations of nanoindentation techniques to characterize the mechanical properties of thin coatings. They considered these nanoindentation systems as ultimate mechanical property microprobes that characterize thin coatings. Nanoindentation technique has been used by Voevodin et al. [2] to evaluate the mechanical properties of diamond-like carbon (DLC) coatings prepared by pulsed laser deposition. There have been numerous analytical and finite element models developed for the nanoindentation of thin coatings. (Knapp et al. [23,24,25], Bouzakis et al. [26], Chudoba et al. [13]). They also conducted nanoindentation experiments for various types of coated systems and developed the procedures for obtaining the mechanical properties of thin coatings based on finite-element modeling of nanoindentation. They emphasized the situation when substrate effects for thin coating mechanical properties measurement are dominant, that is, the thin hard coatings over softer substrates.

In this present study, the elastic plastic finite element analysis model using measured material properties has been developed and used to determine the stress distribution in the FG Ti/TiC/DLC multilayered tribological coating system and examine the elastic plastic deformation of the coating systems during indentation. Due to nanoindentation experiment technique in connection with nanoindentation FEA model simulation, yield strengths of the coating materials were calculated using the measured material properties such as hardness and modulus of elasticity for each coating material.

#### **4.2 Functionally Gradient (FG) Multilayered Tribological Coating**

Voevodin et al. [3] illustrated the need for the functionally gradient (FG) multilayered tribological coatings in heavily loaded contact applications and developed the multilayered FG Ti/TiC/DLC coating system shown in Figure 3.1. Instead of having diamond like carbon (DLC) coating on top of the substrate, there is Ti/TiC coating system that has gradual Ti and C composition changes to improve the load support and adhesion between the DLC coating and the substrate.

#### 4.2.1 Nanoindentation

To measure the material properties such as hardness and modulus of elasticity for FG Ti/TiC/DLC coating system, a MTS nano indenter® XP was used for the experiment under the carefully controlled environment. Figure 3.2 depicts the schematic of nanoindentation for multilayered semi-infinite medium with a spherical indenter tip. The spherical indenter tip is loaded vertically during nanoindentation. It is assumed that gradient coatings have a series of perfectly bonded block layers with unique material properties and layer thickness. However, the gradient coatings don't have distinct layers in reality. They normally have continuous gradual change of Ti and C composition. It is also assumed that there is no interfacial stress generated by the deposition process at the interfaces. In order to develop an accurate nanoindentation model for the FG Ti/TiC/DLC coating system, material property measurements for the inputs to the FEA model are required. It is difficult to measure the material properties for each distinct layer from the FG multilayered coating system because the material property measurements for thin coatings require very sophisticated instruments due to the magnitude of coating thickness. Nano indenters with nano-Newton resolution in loading and nano-meter resolution in displacement allow very accurate measurements of the load-displacement curve for the thin coatings. Figure 4.1 demonstrates a portion of two dimensional axi-symmetric FEA model of the nanoindentation simulation using a conical indenter tip for coating samples. This FEA model was used for various coating samples to calculate their yield strengths of thin coatings using measured hardness (H) and modulus of elasticity (E) data. Knapp et al. [23] developed the two dimensional axi-symmetric FEA model with the shape of the conical indenter tip to verify that the conical tip with a certain angle has the same area versus depth relationship for the Berkovich indenter tip. A diamond Berkovich tip was used for the nanoindentation experiments to measure the hardness and modulus of elasticity of thin coatings. Since the hardness of thin coating materials are relatively high, the deformation of the diamond indenter tip is not avoidable. Therefore, the deformable indenter tip was used for the FEA model. Each coating sample consists of 1  $\mu\text{m}$  thick coating and 440C stainless steel substrate. The area function for the Berkovich indenter tip was calibrated through a series of nanoindentation onto fused silica sample. Nanoindentation experiment was performed for the carefully prepared samples to minimize the measurement errors.





Although there are no measured yield strength results from nanoindentation experiments, by the aid of the numerical nanoindentation simulation using a FEA model, the yield strengths of thin coatings are able to be calculated.

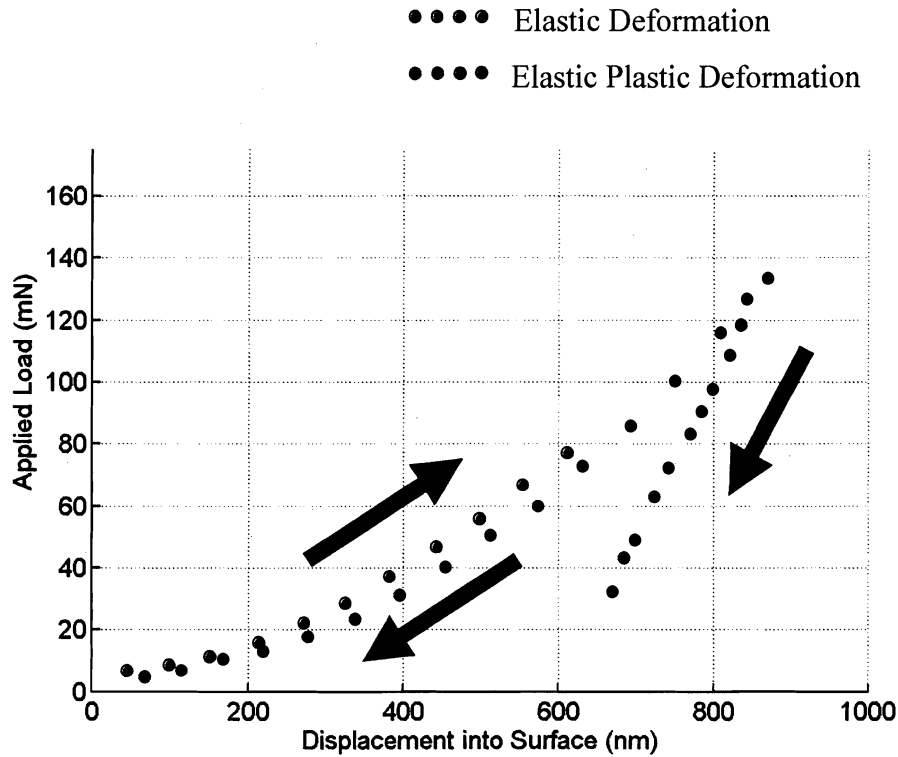


**Figure 4.2. Load vs. displacement curves for elastic deformation and elastic-plastic deformation from nanoindentation experiment respectively.**

Therefore, interactive procedure between FEA model simulations and nanoindentation experiments is required to calculate the yield strengths of the thin coating materials. It is assumed that the plastic deformation of a coating is initiated when its von Mises stress generated inside the coating becomes greater than yield strength of the coating material.

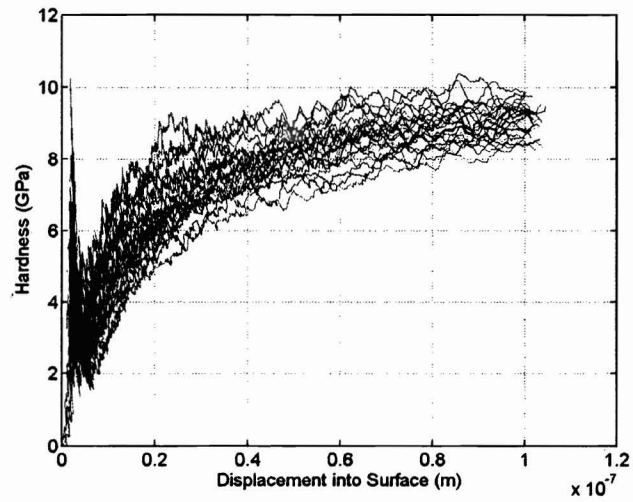
## **4.3 Results and Discussion**

### **4.3.1 Yield Strength Calculation Procedure**

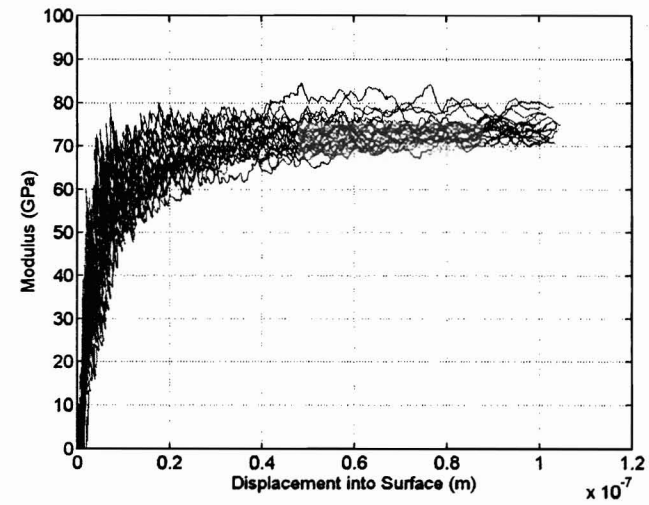
The procedure to calculate yield strength of a coating material is the following. The measurement of TiC/DLC coating material properties such as hardness and modulus of elasticity was conducted using a MTS nano indenter with a Berkovich indenter tip. The measured modulus of elasticity of the coating material is used as an input to the FEA model for the nanoindentation simulation. Also, yield strength of the coating material should be used as an input for the nanoindentation simulation. The initial yield strength of the coating material is

guessed based on the measured hardness value of the material. This step requires an iterative procedure to obtain a best-fit load vs. displacement curve from the nanoindentation simulation by changing the yield strength input value for the simulation. Therefore, when the computational best-fit load vs. displacement curve matches the experimental averaged load vs. displacement curve closely, the guessed yield strength value is considered as the yield strength of the material. Yield strength of each sample is determined from the nanoindentation simulation.

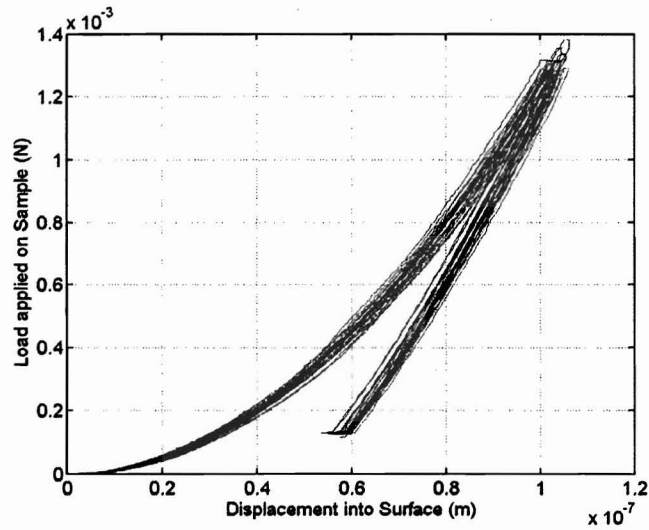
To calibrate the indenter tip area function, a series of indentation was performed on fused silica ( $\text{SiO}_2$ ) because  $\text{SiO}_2$  is a standard material for nanoindentation. The indentation depth was limited to 100 nm because each TiC/DLC coating sample has 1  $\mu\text{m}$  coating thickness. To avoid the substrate effect on the material property measurement of thin coating materials, 1/10 rule was applied. Twenty five indentation tests were performed on the  $\text{SiO}_2$  with 100 nm indentation depth. The nanoindentation experiment results for  $\text{SiO}_2$  are in shown Figures 4.3 (a) through 4.3 (d). Figure 4.3(a) depicts the hardness vs. displacement curves for  $\text{SiO}_2$ . The measured average value for the hardness of  $\text{SiO}_2$  is  $8.9 \pm 0.4$  GPa. Figure 4.3(b) demonstrates the modulus of elasticity vs. displacement curves for  $\text{SiO}_2$ . The measured average value for modulus of elasticity of  $\text{SiO}_2$  is  $72.3 \pm 3.5$  GPa. Hardness values were taken at the maximum penetration depths, and moduli of elasticity were calculated from the upper unloading portions of the load-displacement curves (Voevodin et al., [3]). Figure 4.3(c) illustrates the load vs. displacement curves of  $\text{SiO}_2$  corresponding to the hardness and modulus of elasticity curves of  $\text{SiO}_2$ . During loading,  $\text{SiO}_2$  deforms elastically and then yields. During unloading, the elastic deformation of  $\text{SiO}_2$  is recovered while the plastic deformation remains as a permanent impression on the contact surface. The load vs. displacement curve comparison between the experimental results and FEA results on  $\text{SiO}_2$  is shown in Figure 4.3(d). The yield strength value of  $\text{SiO}_2$  was determined by FEA model nanoindentation simulation. Since the measured average modulus of elasticity of  $\text{SiO}_2$  is 72.3 GPa from nanoindentation test, 72.3 GPa is used as an input value to FEA model simulation for  $\text{SiO}_2$ . Circles show the load vs. displacement curve using average nanoindentation experimental results. The best-fit solid line is obtained through the FEA nanoindentation model simulation.  $Y = 7.1$  GPa and  $E = 72.3$  GPa were used for the inputs to nanoindentation simulation because  $Y = 7.1 \pm 0.3$  GPa and  $E = 73 \pm 0.5$  GPa were found in the literature (Knapp et al., [25]). The results indicate that the best-fit load vs. displacement curve from FEA model



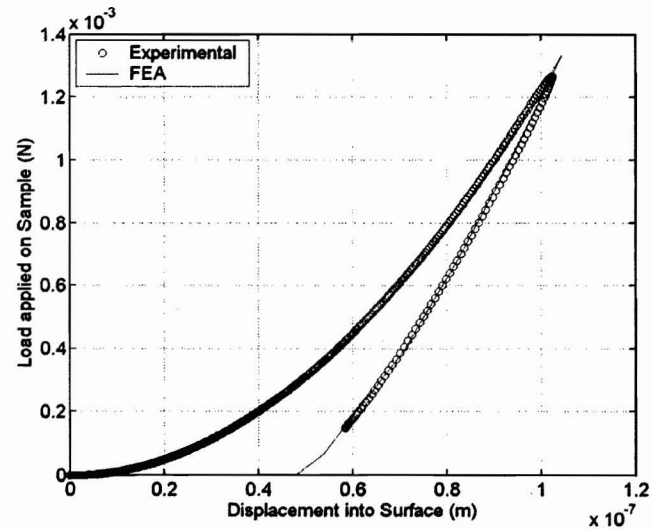
(a)



(b)



(c)

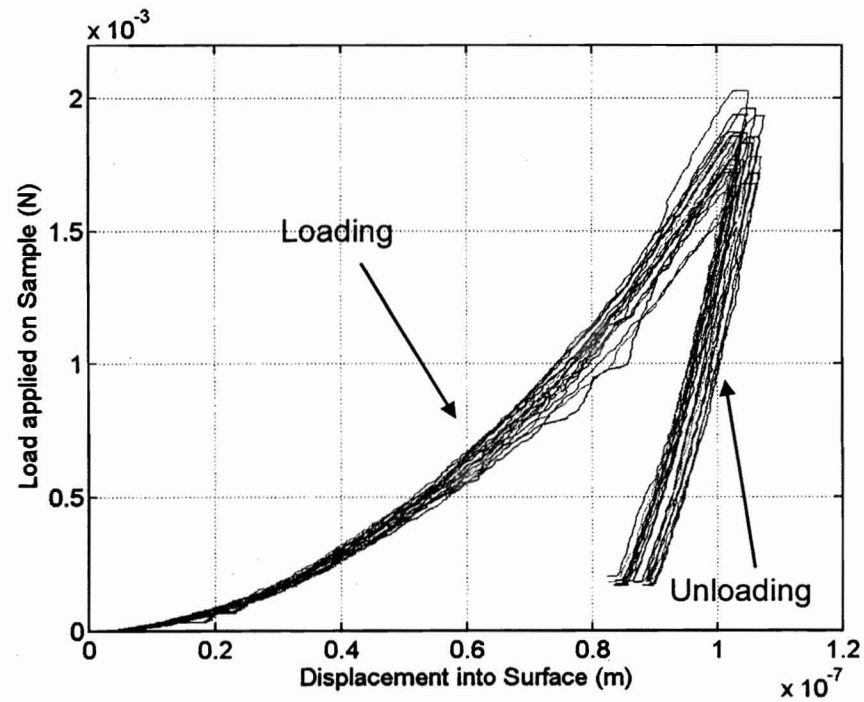


(d)

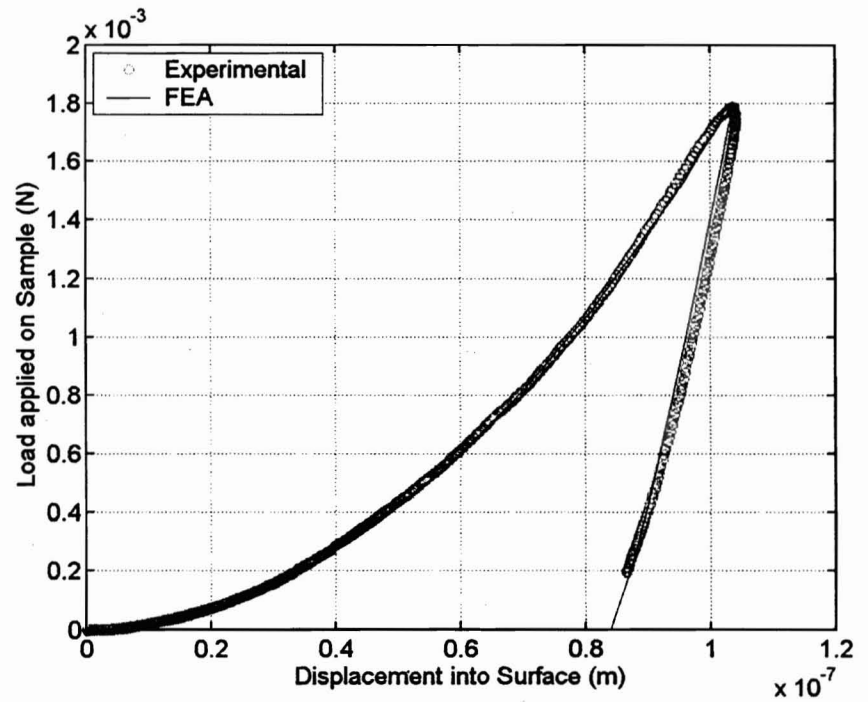
**Figure 4.3. Nanoindentation results for SiO<sub>2</sub>; (a) hardness vs. displacement plot, (b) modulus of elasticity vs. displacement plot, (c) load vs. displacement plot, and (d) load vs. displacement plot for experimental results and FEA results.**

simulation agrees well with the average load vs. displacement curve from the nanoindentation experiment.

Nanoindentation experiments were conducted for 440C stainless steel because 440C stainless steel is used for the substrate of all Ti/TiC/DLC coating samples. Figure 4.4(a) shows the load vs. displacement curves for 440C stainless steel during loading and unloading stages of nanoindentation. Due to the surface roughness of 440C stainless steel, experimental curves are scattered. Because of the nature of the 440C stainless steel, higher load,  $\sim 1.8$  mN, was required to make indentations upto 100 nm in depth than  $\text{SiO}_2$ . Also, the slope of the load vs. displacement curves during unloading for 440C stainless steel is steeper than the slope of the load vs. displacement curves during unloading for  $\text{SiO}_2$ . Figure 4.4(b) displays the comparison of load vs. displacement curves between the average experimental results and the best-fit FEA results. The average experimental load vs. displacement curve matches the best-fit computational load vs. displacement curve when  $Y = 4.0$  GPa and  $E = 220$  GPa are used.



(a)



(b)

**Figure 4.4. Nanoindentation results for 440C stainless steel; (a) load vs. displacement plot and (b) comparison of load vs. displacement plot between average experimental results and best-fit simulation results.**

### 4.3.2 Nanoindentation for Ti/TiC/DLC Coating Material Properties

TiC/DLC coating samples were prepared by a hybrid of magnetron sputtering and pulsed laser deposition. Crystalline  $\alpha$ -Ti, TiC and amorphous DLC films were formed at 100 °C substrate temperature by varying film composition. X-ray photoelectron spectroscopy (XPS) was performed on the coatings for the characterization (Voevodin et al., [2]). Figure 4.5 shows the schematic of nanoindentation on coating sample to measure the material properties. Vertical displacement of the indenter tip is applied to the sample during the nanoindentation. The nanoindentation process was simulated by moving the indenter tip vertically with controlled displacement while calculating reaction force at the contacted area. 440C stainless steel is used as a substrate for all coating samples that have 1  $\mu\text{m}$  thick coating deposited. For the simulation, the coefficient of friction between the indenter tip and sample surface varies from 0.0 to 1.0. Table 4.1 consists of the measured material properties such as the modulus of elasticity and hardness for TiC/DLC coating samples. The results indicate that the hardness and modulus of elasticity changes drastically as Ti and C composition changes.

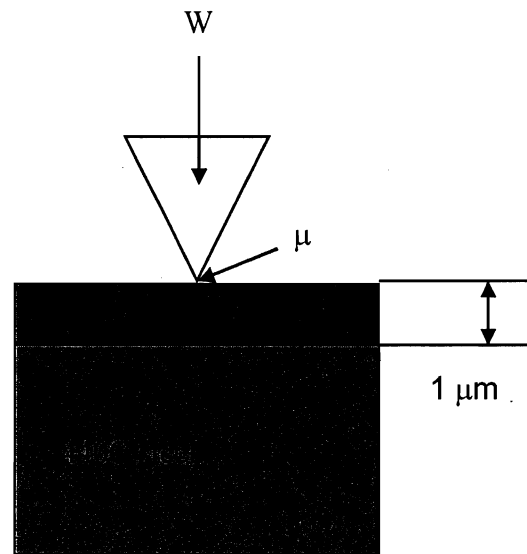


**Figure 4.5. Schematic of nanoindentation with a Berkovich indenter tip on coating samples such as Ti,  $\text{Ti}_{1-x}\text{C}_x$ , and DLC on 440C stainless steel to measure the material properties.**

The experimental results for  $\text{Ti}_{.53}\text{C}_{.47}$  coating from nanoindentation are shown in figures 4.6(a) through 4.6(d). The indentation depth to  $\text{Ti}_{.53}\text{C}_{.47}$  coating sample is limited to 100 nm to avoid the substrate effect on measured material properties. The figure 4.6(a) shows scattered data for hardness vs. displacement curves because of the surface roughness effect on the measurement. The hardness increases as the nanoindentation depth increases for  $\text{Ti}_{.53}\text{C}_{.47}$

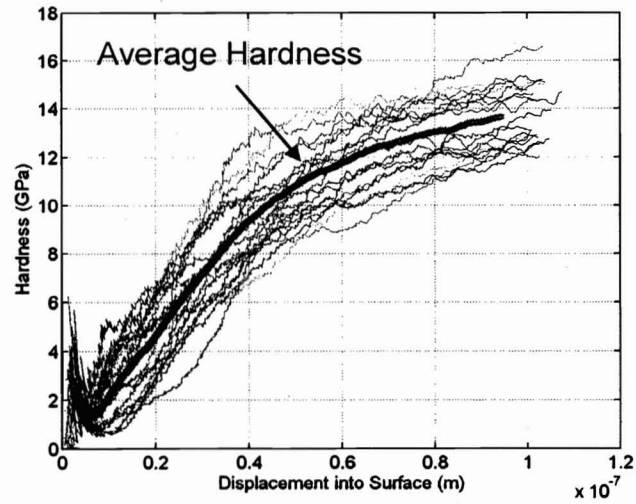
coating. The average hardness of  $\text{Ti}_{.53}\text{C}_{.47}$  coating from the nanoindentation experiments is  $14.2 \pm 1.8$  GPa. The thick solid line represents the average hardness value of  $\text{Ti}_{.53}\text{C}_{.47}$  coating along the indentation depth. The figure 4.6(b) depicts the modulus of elasticity vs displacement curves for  $\text{Ti}_{.53}\text{C}_{.47}$  coating. The average modulus of elasticity of  $\text{Ti}_{.53}\text{C}_{.47}$  coating is  $231.1 \pm 34.6$  GPa. The thick solid line shows the average value of the modulus of elasticity for  $\text{Ti}_{.53}\text{C}_{.47}$  coating along the indentation depth. The figure 4.6(c) illustrates the load vs. displacement curves for

**Table 4.1. Mechanical material properties such as modulus of elasticity (E) and hardness (H) for TiC/DLC coating samples.**

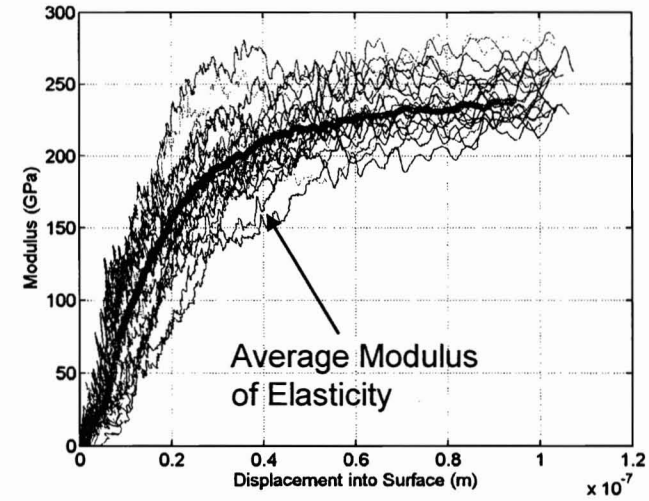
| Samples                         | Material Properties                                  |
|---------------------------------|--|
| DLC at $2 \times 10^{-1}$ Pa    | $E = 350$ GPa, $H = 33$ GPa                          |
| $\text{Ti}_{.19}\text{C}_{.81}$ | $E = 230$ GPa, $H = 13$ GPa                          |
| $\text{Ti}_{.28}\text{C}_{.72}$ | $E = 280$ GPa, $H = 22$ GPa                          |
| $\text{Ti}_{.53}\text{C}_{.47}$ | $E = 240$ GPa, $H = 14$ GPa                          |
| $\text{Ti}_{.90}\text{C}_{.10}$ | $E = 145$ GPa, $H = 4.5$ GPa                         |
| 440C stainless steel            | $E = 220$ GPa, $H = 9$ GPa, $\sigma_y = 4$ GPa (FEA) |

$\text{Ti}_{.53}\text{C}_{.47}$  coating from nanoindentation. Due to the roughness of surface, the data is scattered. The figure 4.6(d) shows the comparison of averaged experimental results and best-fit FEA results for  $\text{Ti}_{.53}\text{C}_{.47}$  coating. The average load vs. displacement curve agrees well with best-fit load vs. displacement curve when  $Y = 10$  GPa and  $E = 240$  GPa are used for  $\text{Ti}_{.53}\text{C}_{.47}$  coating nanoindentation simulation.

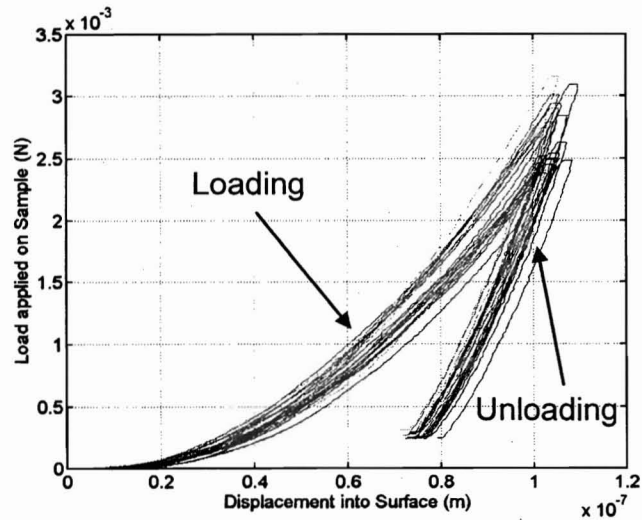




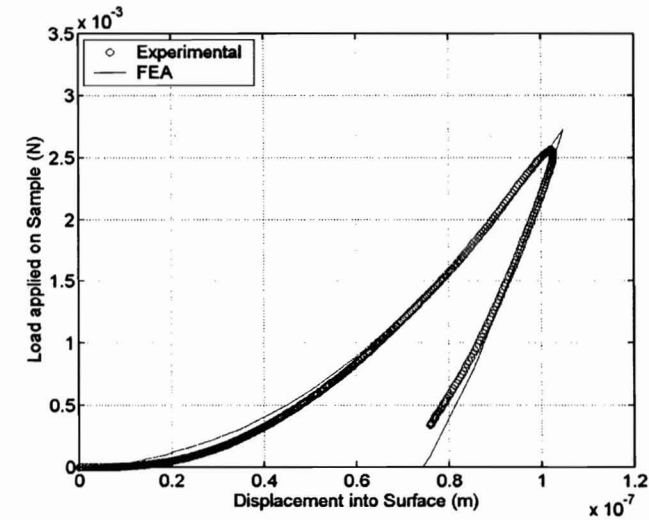
(a)



(b)



(c)



(d)

**Figure 4.6. Nanoindentation results for  $\text{Ti}_{53}\text{C}_{47}$  coating; (a) hardness vs. displacement plot, (b) modulus of elasticity vs. displacement plot, (c) load vs. displacement plot during loading and unloading stages, and (d) comparison of measured average load vs. displacement curve and best-fit load vs. displacement curve from experiments and FEA simulations, respectively.**

Figure 4.7 demonstrates the schematic of functionally gradient (FG) Ti/TiC/DLC coating system design with programmed variation of compositional and mechanical properties proposed by Voevodin et al. [3]. Each layer has its unique material properties and thickness. Hardness and modulus of elasticity of Ti/TiC/DLC coating system are measured from coating samples. 25 indentation locations per sample were averaged to obtain the statistical values. The yield strength for each coating material is calculated from FEA nanoindentation simulation using the measured hardness and modulus of elasticity. These are the values used for inputs to FEA model for this study. The material properties of each layer were linearly interpolated from the measured material properties data. To improve adhesion between the substrate and upper carbide layers,  $\alpha$ -Ti is used as a bond layer.

| Material                         | Hardness | Elastic Modulus | Yield Strength | Thickness | Poisson's Ratio |
|----------------------------------|----------|-----------------|----------------|-----------|-----------------|
| DLC at $10^{-5}$ Pa              | 70 GPa   | 650 GPa         | 45 GPa         |           | 0.1             |
| DLC at $2 \times 10^{-1}$ Pa     | 33 GPa   | 350 GPa         | 28 GPa         |           | 0.1             |
| Ti <sub>10</sub> C <sub>90</sub> | 14 GPa   | 180 GPa         | 9 GPa          |           | 0.15            |
| Ti <sub>25</sub> C <sub>75</sub> | 21 GPa   | 260 GPa         | 14 GPa         |           | 0.15            |
| Ti <sub>30</sub> C <sub>70</sub> | 24 GPa   | 290 GPa         | 16 GPa         |           | 0.20            |
|                                  |          |                 |                |           |                 |
| Ti <sub>90</sub> C <sub>10</sub> | 5 GPa    | 145 GPa         | 2.5 GPa        | 50 nm     | 0.25            |
| $\alpha$ -Ti                     | 2 GPa    | 130 GPa         | 1.5 GPa        | 50 nm     | 0.25            |
| Substrate                        | 9 GPa    | 220 GPa         | 1 GPa          | 9.5 mm    | 0.3             |

**Figure 4.7. Schematic of the functionally gradient Ti/TiC/DLC coating design with variation of composition, dimension, and mechanical properties.**

#### 4.3.3 Finite Element Analysis Model Results

Figures 4.8(a) and 4.8(b) show a schematic of nanoindentation on FG multilayered coating system with a spherical indenter tip and its corresponding finite element analysis model. Figure 4.8(b) depicts two dimensional axi-symmetric finite element analysis model used for the nanoindentation simulation that consists of loading stage and unloading stage. The radius of the diamond spherical indenter tip is 50  $\mu$ m. Since the hardness of the DLC coating is as high as the

diamond tip, the deformable diamond indenter tip is modeled for the nanoindentation simulation. Although the nominal dimension of the diamond indenter is 50  $\mu\text{m}$  in radius, actual dimension of the diamond indenter is 46.95  $\mu\text{m}$  in radius. ABAQUS/Standard was used to model the nanoindentation simulation on the multilayered FG Ti/TiC/DLC coating system. Due to the symmetry of the system, axi-symmetric model was developed to save the computational time. Also, the outer portion of semi-infinite medium used infinite elements to reduce the computing time. Two different types of elements, four-node bilinear, reduced integration with hourglass control element (CAX4R) and four-node linear one-way infinite element (CINAX4), were used.

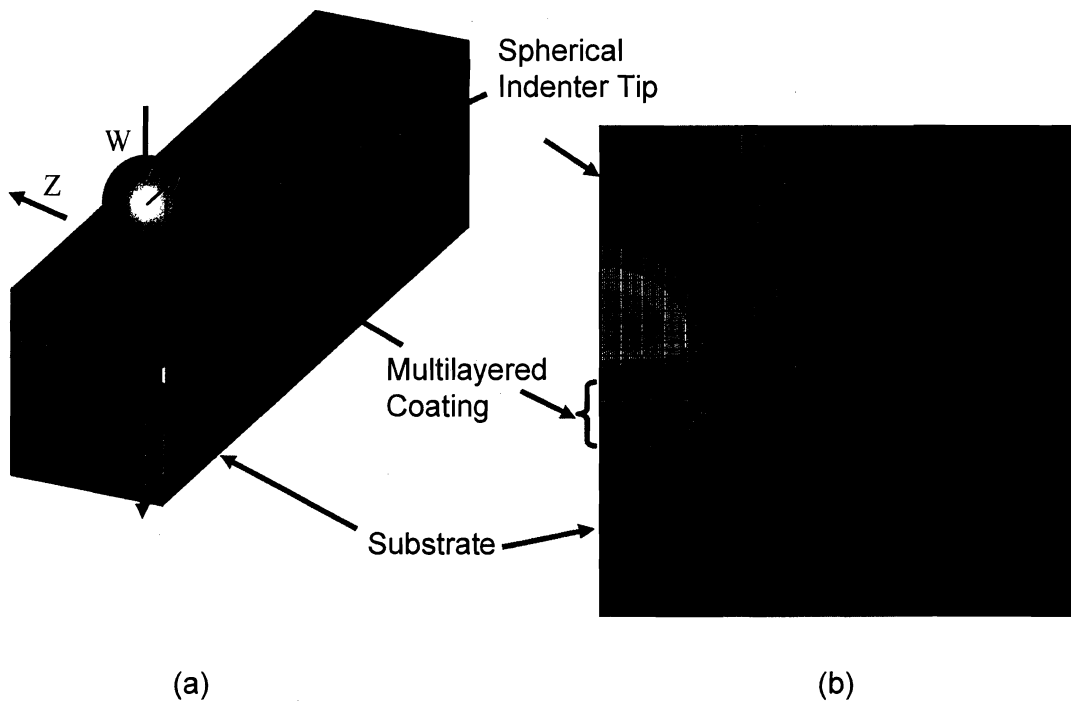


**Figure 4.8. (a) Schematic of nanoindentation on multilayered coating system with a spherical indenter tip, (b) two dimensional axi-symmetric finite element analysis model developed for nanoindentation simulation on a functionally gradient Ti/TiC/DLC multilayered coating system with a spherical indenter tip.**

Figure 4.9(a) shows the effect of multilayered FG Ti/TiC/DLC coating system on von Mises Stress distribution during the nanoindentation for indenter displacement,  $\delta = 50$  nm and friction coefficient,  $\mu = 0.0$ . Figure 4.9(b) describes the schematic of FG multilayered coating system design used for this study. Figure 4.9(a) illustrates the von Mises stress profiles along the depth direction on the plane of symmetry at the center of contact. The dotted line represents the von Mises stress profile along the depth direction for the no coating system case. It shows the

smooth variation of von Mises stress distribution along the depth direction. However, for the multilayered FG Ti/TiC/DLC coating system case, the discrete variation of von Mises stress profile at the interfaces exists. Inside the DLC coatings and FG TiC coatings, higher von Mises stresses were generated than the no coating case because of the higher moduli of elasticity for the DLC and TiC coating materials. If more distinct layers are used for the FG multilayered FEA model, the von Mises stress profile along the depth direction would be smoother, that is,  $Ti_{.85}$ ,  $Ti_{.75}$  and  $Ti_{.65}$  are used.

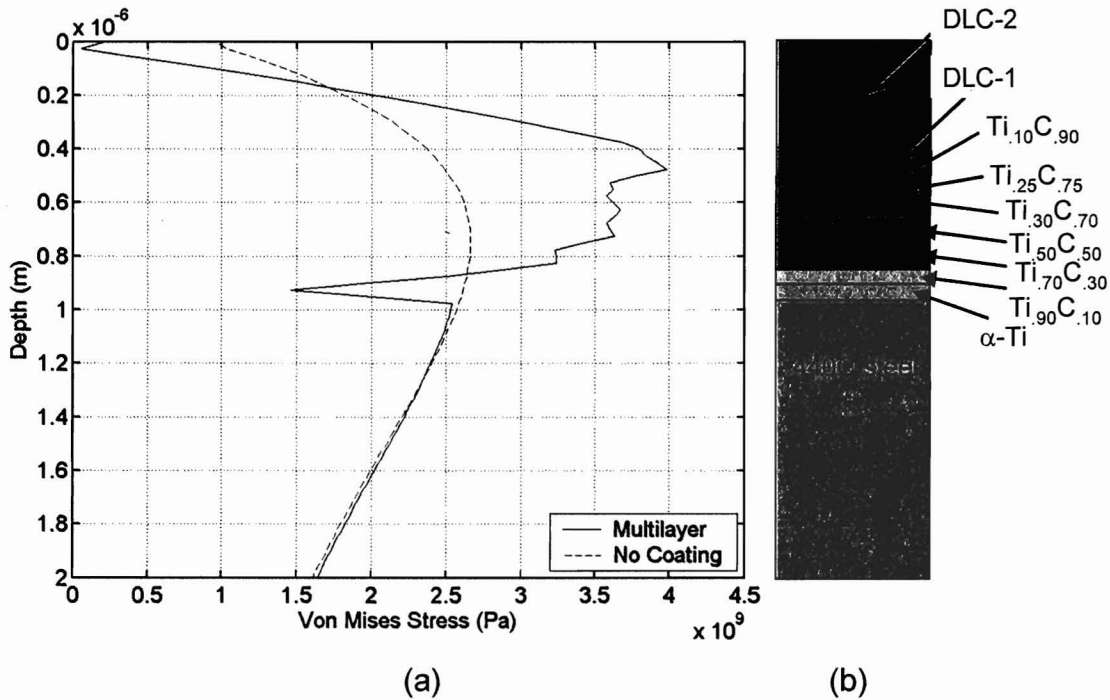
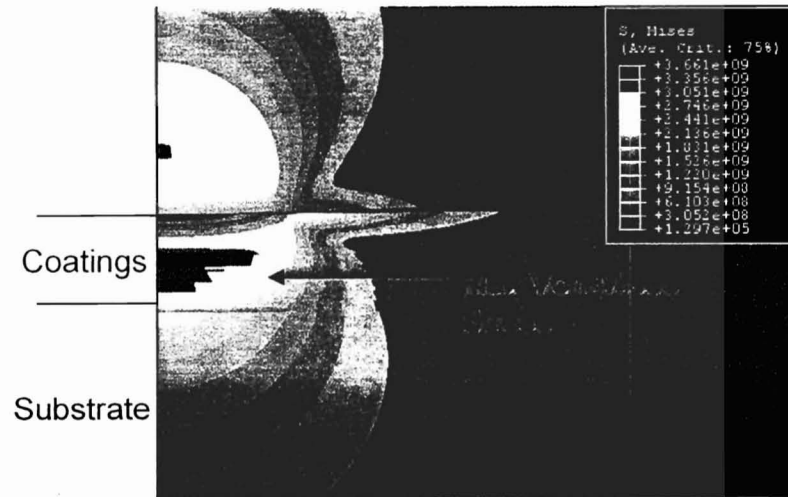


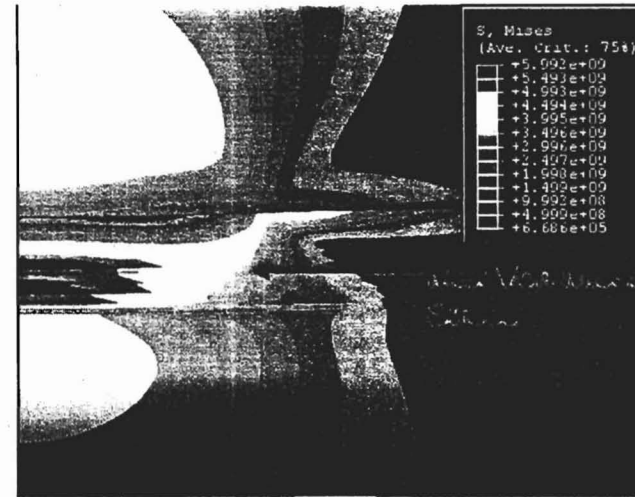
**Figure 4.9. Effect of multilayered FG Ti/TiC/DLC coating system on von Mises stress distribution for the indentation depth,  $\delta = 50$  nm, and coefficient of friction,  $\mu = 0.0$ .**

Figures 4.10(a) through 4.10(d) show contour plots of the von Mises stress distributions for various indenter displacement depths,  $\delta = 40$  nm, 80 nm, 120 nm, and 160 nm at the end of loading stage. The indenter displacement,  $\delta = 40$  nm, generates the maximum Hertzian pressure,  $P_h = 4.5$  GPa, at the contact for no coated elastic 440C stainless steel substrate. The indenter displacement,  $\delta = 160$  nm, generates the maximum Hertzian pressure,  $P_h = 9.0$  GPa, at the contact for no coated elastic 440C stainless substrate. Figure 4.10 (a) depicts the contour plot of von Mises stress distribution inside the FG multilayered coating system generated at the indenter displacement depth,  $\delta = 40$  nm. The maximum von Mises stress, 3.64 GPa, occurs inside the FG TiC/DLC coating system. Figure 4.10 (b) displays the contour plot of von Mises stress

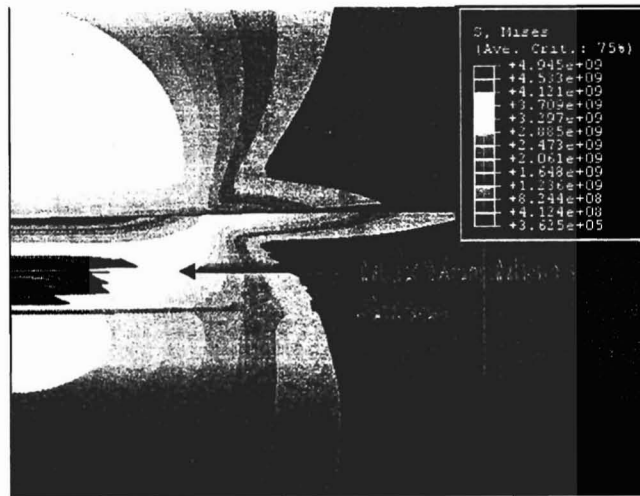
distribution inside the FG multilayered coating system generated at the indenter displacement depth,  $\delta = 80$  nm. The increase of the indenter displacement moves the maximum location of von Mises stress further below the contact surface. The wider contact width is generated due to the increase of the indenter displacement. The maximum von Mises stress, 4.89 GPa, occurs inside the FG TiC/DLC coating system. Figure 4.10 (c) demonstrates the contour plot of von Mises stress distribution inside FG multilayered coating system generated at the indenter displacement depth,  $\delta = 120$  nm. The maximum von Mises stress, 5.93 GPa, occurs inside the FG TiC/DLC coating system. Figure 4.10 (d) illustrates the contour plot of von Mises stress distribution inside FG multilayered coating system generated at the indenter displacement,  $\delta = 160$  nm. Due to the magnitude of the yield strength of the 440C stainless steel substrate, plastic deformation of the substrate occurs. The maximum von Mises stress, 6.57 GPa, occurs inside the FG TiC/DLC coating system. Although the indenter displacement increases from  $\delta = 40$  nm to  $\delta = 160$  nm, the location of maximum von Mises stress generated at the contact remains inside DLC coatings. Also, as the indenter displacement increases, wider contact width and higher von Mises stress occur.



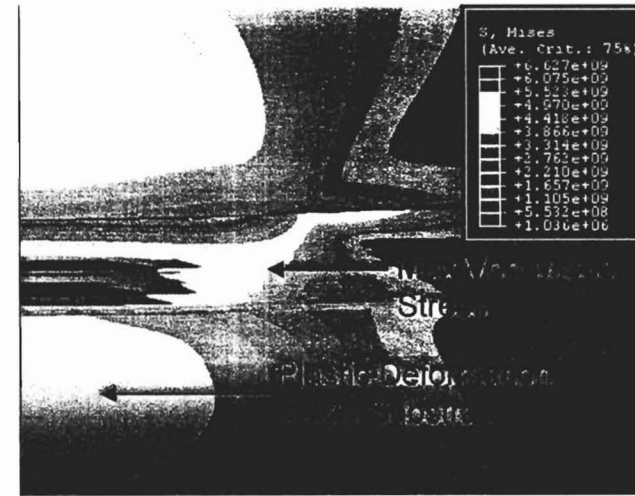
(a)



(b)



(c)



(d)

**Figure 4.10. Contour plots of von Mises stresses distribution generated inside the multilayered FG Ti/TiC/DLC coating system from the FEA model at various indentation depths; (a)  $\delta = 40$  nm, (b)  $\delta = 80$  nm, (c)  $\delta = 120$  nm, and (d)  $\delta = 160$  nm.**

Figures 4.11(a) and 4.11(b) show the von Mises stress distribution for the contact condition,  $\delta = 80$  nm and  $\mu = 0.0$ . Figure 4.11(a) depicts the von Mises stress distribution generated below the center of the contact along the depth direction on the plane of symmetry. Width-axis corresponds to the later surface distance. Depth = 0 represents the surface position. This indicates that the maximum von Mises stress occurs below the center of the contact inside DLC multilayered coating. Due to the distinct material properties for each coating layer, the von Mises stress distribution displays sharp stress changes at the interface. Figure 4.11 (b) illustrates the contour plot of von Mises stress distribution generated inside the multilayered FG Ti/TiC/DLC coating system.

Max. Von Mises Stress occurs inside Multilayered Coating

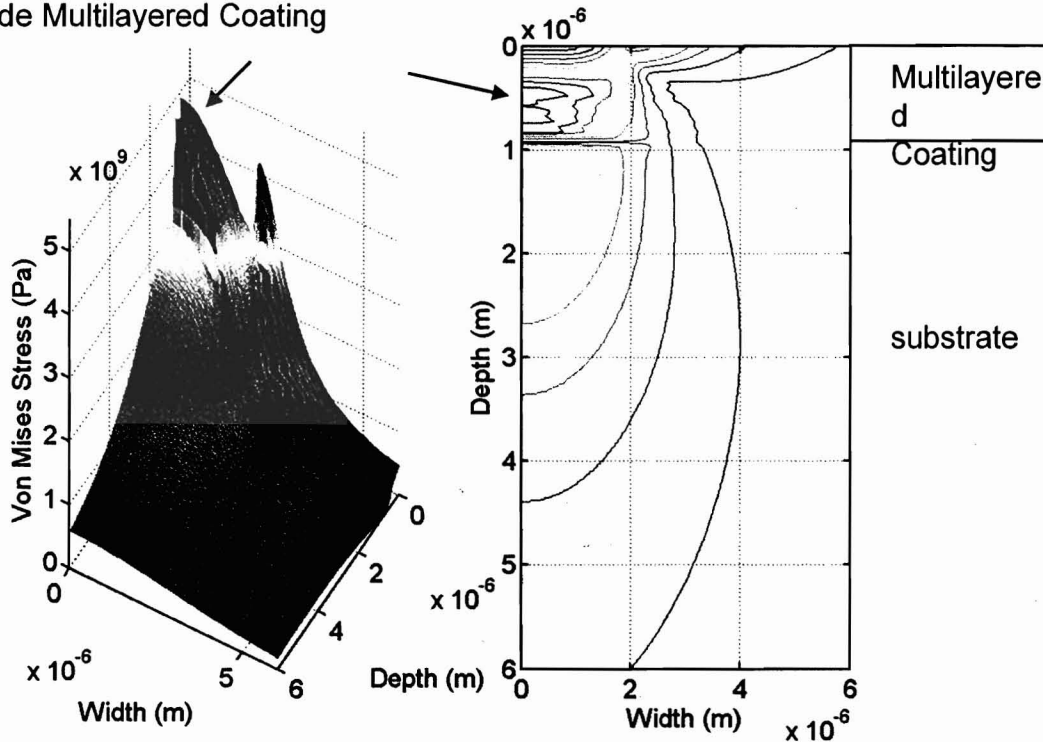
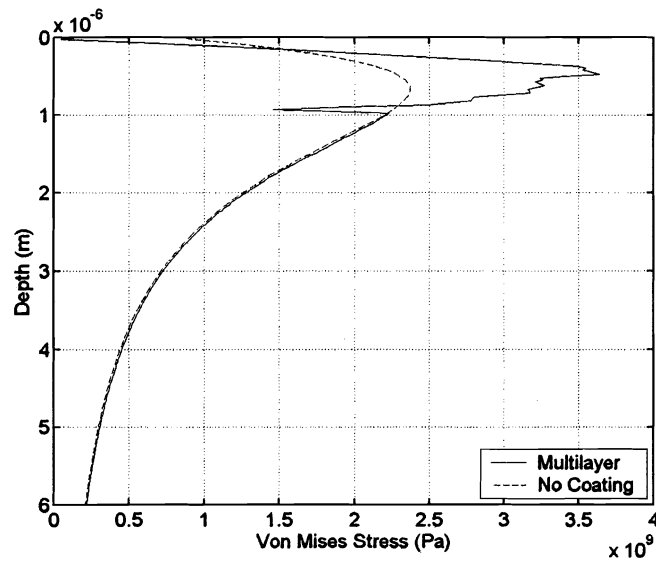


**Figure 4.11. (a) Von Mises stress distribution on the plane of symmetry generated inside the multilayered FG Ti/TiC/DLC coating system for the indentation depth,  $\delta = 80$  nm and coefficient of friction,  $\mu = 0.0$  and (b) contour plot of Von Mises stress distribution.**

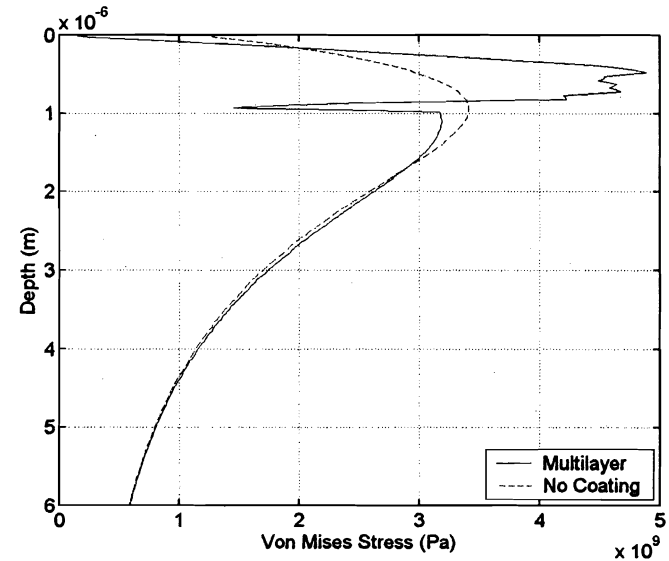
Figures 4.12(a) through 4.12(d) show the effect of applied load on von Mises stress profiles at various indentation depths for the contact condition,  $\mu = 0.0$ . Figure 4.12 (a) depicts the von Mises stress profiles along the depth direction at the center of the contact for indentation depth,  $\delta = 40$  nm, for both FG coated system and 440C stainless steel substrate. Without any coating on the 440C stainless steel substrate, the substrate has a smooth transition of von Mises

stress profile along the depth direction with maximum 2.37 GPa located below the surface. However, the multilayered FG Ti/TiC/DLC coating system has a drastic transition of von Mises stress profile along the depth direction. Especially maximum von Mises stress, 3.64 GPa, occurs at the TiC/DLC interface. Also, the minimum von Mises stress occurs at the bond layer with 1.46 GPa. Figure 4.12 (b) displays the von Mises stress profiles along the depth direction at the center of the contact for indentation depth,  $\delta = 80$  nm. Without any coating on the 440C stainless steel substrate, the substrate has a smooth transition of von Mises stress profile along the depth direction with maximum 3.41 GPa below the contact surface. Due to the higher moduli of elasticity for TiC/DLC materials than 440C stainless steel, the von Mises stress generated inside the FG TiC/DLC coating system has much higher values than no coating case. The FG Ti/TiC/DLC coating system has a drastic transition of von Mises stress along the depth direction. Especially maximum von Mises stress, 4.89 GPa, occurs at the TiC/DLC interface. Also, the minimum von Mises stress occurs at the bond layer with 1.46 GPa. The stress generated at the bond layer interface does not exceed the yield strength of the  $\alpha$  - Ti bond layer because of the elastic-perfectly plastic stress strain relationship assumption. Figure 4.12(c) shows the von Mises stress profiles along the depth direction at the center of the contact for indentation depth,  $\delta = 120$  nm. Without the FG Ti/TiC/DLC multilayered coating system, the maximum von Mises stress, 4.00 GPa, occurs in the substrate and causes the plastic deformation inside the substrate. The FG TiC/DLC coating system has maximum von Mises stress, 5.93 GPa, at the DLC/TiC interface. At the  $\alpha$ -Ti bond layer, the von Mises stress was limited to 1.46 GPa because of the material properties of  $\alpha$ -Ti layer. Figure 4.12(d) depicts the von Mises stress profiles along the depth direction at the center of the contact for indentation depth,  $\delta = 160$  nm. Without the FG Ti/TiC/DLC multilayered coating, the maximum von Mises stress, 4.00 GPa, occurs in the substrate and causes the larger plastic deformation region inside the substrate. Although there is the FG Ti/TiC/DLC multilayered coating system, von Mises stress, 4.00 GPa, occurs inside the substrate and causes the plastic deformation region inside the substrate. The FG TiC/DLC coating system has maximum von Mises stress, 6.57 GPa, at the DLC/TiC interface. At the  $\alpha$ -Ti bond layer, the von Mises stress was limited to 1.46 GPa because of the material properties of  $\alpha$ -Ti layer. This indicates the

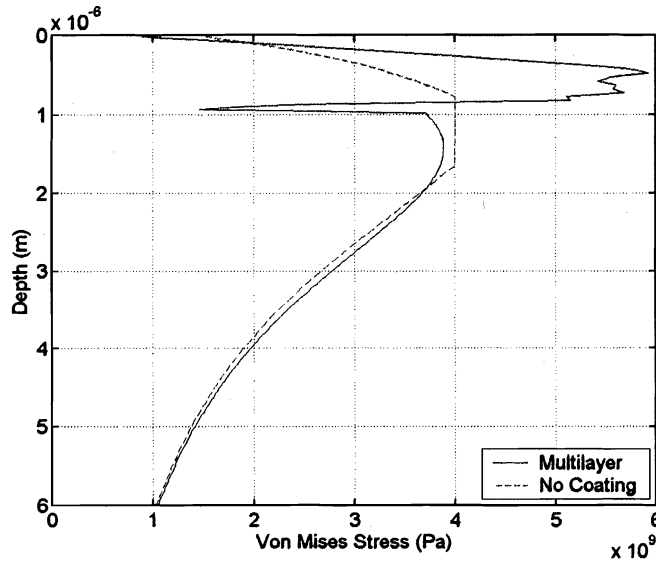




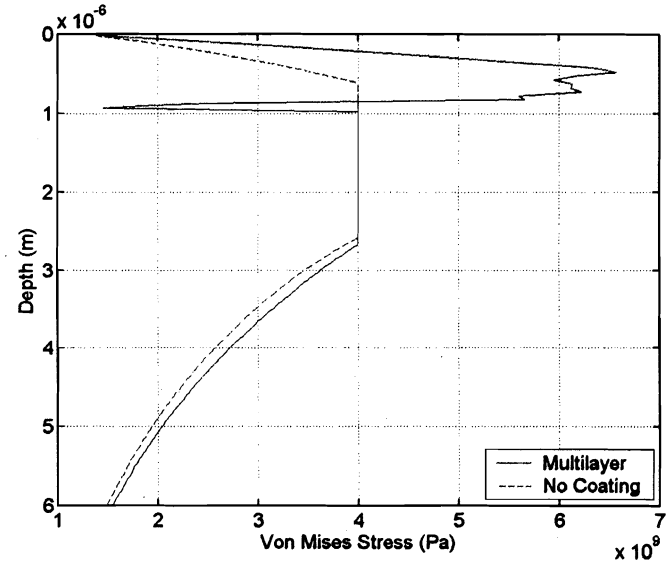
(a)



(b)



(c)



(d)

**Figure 4.12.** Effect of applied load on von Mises stresses profiles along the depth direction at the center of the contact at various indentation depths for friction coefficient,  $\mu = 0.0$ ; (a)  $\delta = 40$  nm, (b)  $\delta = 80$  nm, (c)  $\delta = 120$  nm, and (d)  $\delta = 160$  nm.

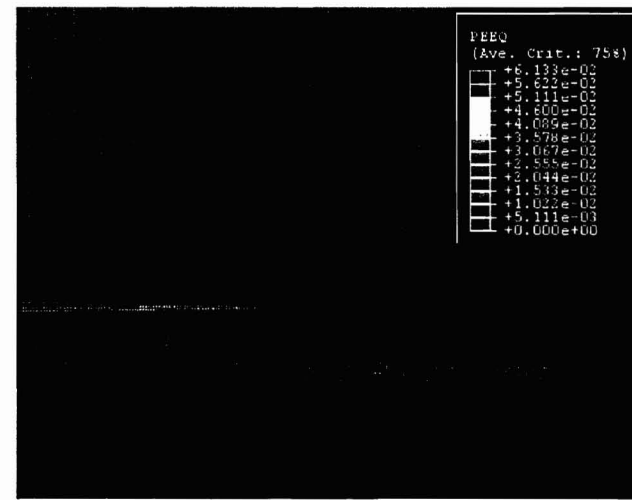
effect of bond layer on the von Mises stress distribution, that is, there are significant changes of von Mises stress magnitude at the bond layer. Generally stress profile shape remains the same. However, the magnitude of von Mises stress increases as the indenter displacement increases.

Figures 4.13(a) through 4.13(d) show the contour plots of equivalent plastic strain distribution generated for FG multilayered coating system from the FEA model at various indentation depths. Figure 4.13 (a) illustrates contour plot of the equivalent plastic strain distribution generated inside the FG multilayered coating system at the end of loading stage. The figure indicates that the maximum equivalent plastic strain occurs at the  $\alpha$ -Ti bond layer for the indenter displacement,  $\delta = 40$  nm. The plastic strain was initiated at the  $\alpha$ -Ti bond layer below the center of the contact with the maximum magnitude of  $9.875 \times 10^{-3}$ . Figure 4.13 (b) depicts the contour plot of equivalent plastic strain distribution generated inside the FG multilayered coating system for the indenter displacement,  $\delta = 80$  nm. As the indenter displacement increases, the magnitude of the equivalent plastic strain is increased to  $6.133 \times 10^{-2}$  at the  $\alpha$ -Ti bond layer. The location of the maximum equivalent plastic strain moves from the center of the contact to the edges of the contact. Figure 4.13 (c) demonstrates the contour plot of equivalent plastic strain distribution generated inside the FG multilayered coating system for the indenter displacement,  $\delta = 120$  nm. As the indenter displacement increases, the magnitude of the equivalent plastic strain is increased to  $1.611 \times 10^{-1}$ . The location of the maximum equivalent plastic strain moves further from the axis of symmetry to the edges of the contact. Figure 4.13 (d) displays the contour plot of equivalent plastic strain distribution generated at the  $\alpha$ -Ti bond layer for indenter displacement,  $\delta = 160$  nm. As the indenter displacement increases, the magnitude of the equivalent plastic strain is increased to  $2.598 \times 10^{-1}$ . The location of the maximum equivalent plastic strain moves further from the center of the contact to the edges of the contact, i.e. the half contact width.

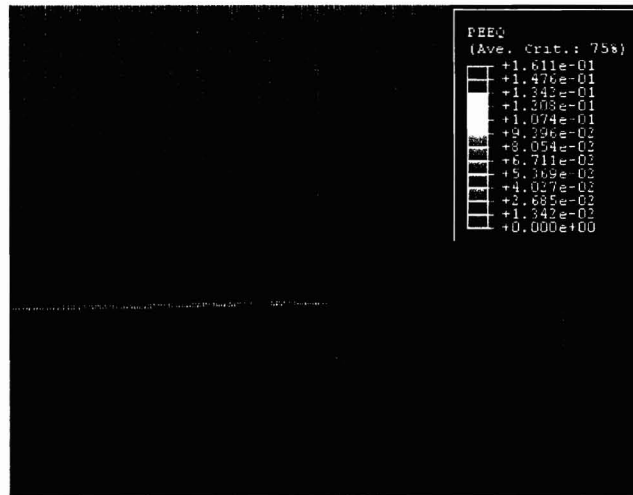
During the nanoindentation process, the multilayered FG Ti/TiC/DLC coating system still experiences the residual stress after the nano indenter tip is unloaded from the FG multilayered coating system. Figures 4.14(a) through 4.14(d) show the contour plots of residual von Mises stress distribution generated inside the multilayered FG Ti/TiC/DLC coating system obtained from the FEA model. As the indenter tip displacement increases, the multilayered FG Ti/TiC/DLC coating system shows the higher residual von Mises stresses generated inside the



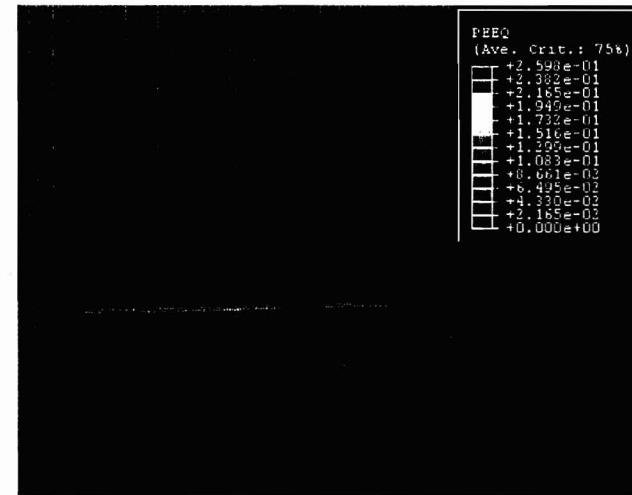
(a)



(b)

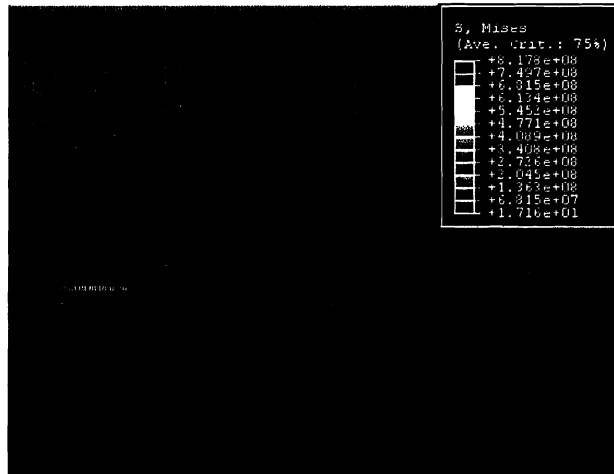


(c)

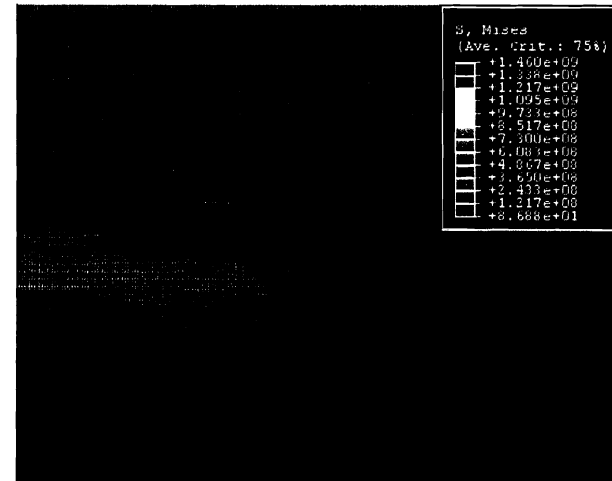


(d)

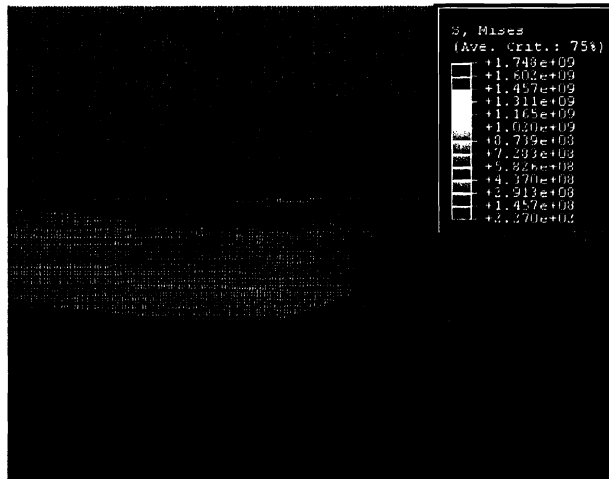
**Figure 4.13. Contour plots of equivalent plastic strain distribution generated on the plane of symmetry inside the multilayered FG Ti/TiC/DLC coating system at various indentation depths; (a)  $\delta = 40$  nm, (b)  $\delta = 80$  nm, (c)  $\delta = 120$  nm, and (d)  $\delta = 160$  nm.**



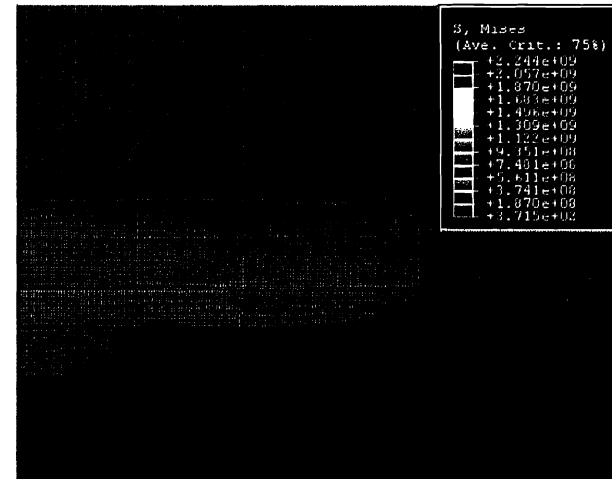
(a)



(b)



(c)



(d)

**Figure 4.14. Contour plots of residual von Mises stress distribution generated inside multilayered FG Ti/TiC/DLC coating system after the unloading of nano indenter tip from various indentation depths; (a)  $\delta = 40$  nm, (b)  $\delta = 80$  nm, (c)  $\delta = 120$  nm, and (d)  $\delta = 160$  nm.**

coating system. Figure 4.14 (a) depicts the contour plot of residual von Mises stress distribution after the indenter displacement,  $\delta = 40$  nm, is applied and removed. The maximum residual von Mises stress,  $8.178 \times 10^8$  Pa, is generated below the center of the contact. The location of the maximum residual stress is at the  $\alpha$ -Ti bond layer. Figure 4.14 (b) demonstrates the contour plot of residual von Mises stress distribution inside the Ti/TiC/DLC coating system after the indenter displacement,  $\delta = 80$  nm, is applied and removed. The maximum residual von Mises stress generated below the contact is  $1.460 \times 10^9$  Pa around the  $\alpha$ -Ti bond layer. As the indentation depth increases, the larger region below the contact surface is influenced by the residual stress. Figure 4.14 (c) illustrates the contour plot of residual von Mises stress distribution inside the Ti/TiC/DLC coating system after the indenter displacement,  $\delta = 120$  nm, is applied and removed. The maximum von Mises stress generated below the contact is  $1.748 \times 10^9$  Pa around the  $\alpha$ -Ti bond layer. Figure 4.14 (d) displays the contour plot of residual von Mises stress distribution inside the Ti/TiC/DLC coating system after the indenter displacement,  $\delta = 160$  nm, is applied and removed. The maximum residual von Mises stress generated below the contact is  $2.244 \times 10^9$  Pa around the  $\alpha$ -Ti bond layer. Larger area of the coating system has the residual von Mises stress inside the Ti/TiC/DLC coating system after the indenter tip is load and removed from the contact for the indenter displacement,  $\delta = 160$  nm.

Figure 4.15 shows the effect of coating system design on von Mises stress profiles inside the coating systems along the depth direction at the center of the contact on the plane of symmetry under the contact condition,  $\delta = 200$  nm and  $\mu = 0.0$ . The dashdot line describes the von Mises stress profile variation from the substrate surface to  $0.55 \times 10^{-6}$  m below the substrate surface for the no coated substrate. The magnitude of the von Mises stress increases upto 4 GPa as the depth inside the substrate increases and remains constant due to the yield strength of 440C stainless steel. The dashed line represents the von Mises stress profile variation from the thin DLC coating surface to the substrate. The maximum von Mises stress, 5.67 GPa, occurs at the DLC coating and substrate interface. Also the maximum von Mises stress for the substrate is limited to 4.00 GPa. The dotted line reveals the stress profile variation across thickness of the thick DLC coating and substrate system. The maximum von Mises stress of 10.1 GPa occurs at the DLC coating and substrate interface. Drastic stress profile change occurs at the interface due to the different material properties. The solid line shows the von Mises stress profile variation

generated for the multilayered FG Ti/TiC/DLC coating system. The Ti/TiC/DLC coating system has relatively moderate stress variation across the thickness of the coating system compared to the thick monolayered DLC coating because of the gradually variation of material properties across the thickness of the coating system.

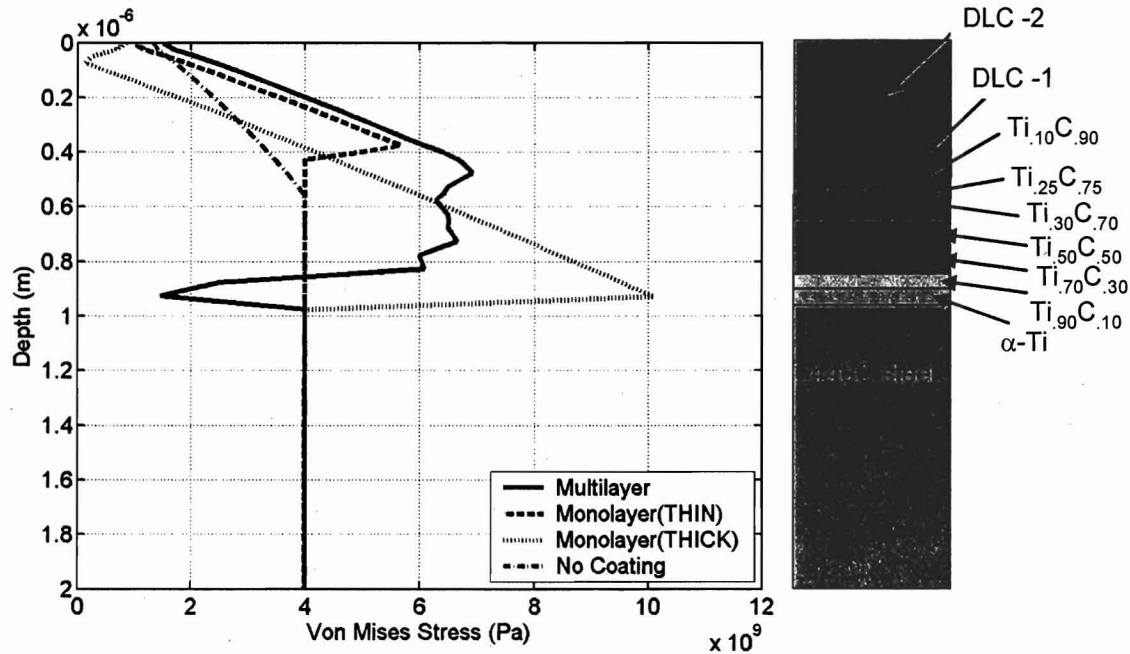


**Figure 4.15. Effect of coating system design on von Mises stress distribution generated inside the coating system for the contact condition,  $\delta = 200$  nm and  $\mu = 0.0$ .**

#### 4.4 Summary and Conclusion

Nanoindentation technique has been used for the mechanical characterization of coating materials. The finite element analysis model extends the usage of nanoindentation technique to the calculation of material property such as yield strength from the experimental nanoindentation data such as hardness and modulus of elasticity. Therefore, nanoindentation simulation by the finite element analysis model has been performed to determine the yield strengths for the multilayered FG Ti/TiC/DLC coating materials based on the measured nanoindentation data. Using the measured and calculated material properties for the coating system, the FEA model has been developed to investigate the stress distribution and elastic-plastic deformation generated inside the multilayered FG Ti/TiC/DLC coating system due to the nanoindentation.

The superiority of the multilayered FG Ti/TiC/DLC coating system at high load applications was shown and discussed. The multilayered FG Ti/TiC/DLC coating system improves the system integrity under the heavy loading condition. It significantly reduces the

magnitude of the maximum von Mises stress generated and the drastic stress profile variation across the thickness of the coating system than monolayered DLC coating system due to the moduli difference of the coating materials. Also, it improves the wear resistance and load support mechanism compared to both no coating system and monolayered DLC coating system. To improve the adhesion between the DLC/TiC coating system and substrate, the bond layer is used. However, due to the material properties of the bond layer materials, bond layers become the prime location of the plastic deformation under the severe high loading condition. The residual stress should be considered as a key design factor when the multilayered FG coating system is developed.

## 5.0 REFERENCES

1. V.V. Lyubimov, A.A. Voevodin, S. E. Spassky and A. L. Yerokhin, 1992, "*Stress Analysis and Failure Possibility Assessment of Multilayer Physically Vapour Deposited coatings*," Thin Solid Films, 207, pp 117-125.
2. A.A. Voevodin, M.S. Donley, J.S. Zabinski, and J.E. Bultman, 1995, "*Mechanical and Tribological Properties of diamond-Like Carbon Coatings Prepared by Pulsed Laser Deposition*," Surface and Coating Technology, 76-77, pp 534-539.
3. A.A. Voevodin, S.D. Walck, and J.S. Zabinski, 1997b, "*Architecture of multilayer Nanocomposite Coatings with super-Hard Diamond-Like Carbon Layers for wear Protection at high Contact Loads*," Wear, 203-204, pp 516-527.
4. A.A. Voevodin, M.A. Capano, S.J.P. Laube, M.S. Donley, and J.S. Zabinski, 1997a, "*Design of A Ti/TiC/DLC functionally Gradient Coating Based on Studies of Structural Transitions in Ti-C thin Films*," Thin Solid Films, 298, pp 107-115.
5. Meijers, P., 1968, "*The Contact Problem of a Rigid Cylinder on an Elastic Layer*," Applied Scientific Research, Vol. 18, pp. 353-383.
6. Gupta, P.K. and Walowit, J.A., 1974, "*Contact Stresses Between an Elastic Cylinder and a Layered Elastic Solid*," ASME Journal of Lubrication Technology, Vol. 96, pp. 250-257.
7. Chiu, Y.P. and Hartnett, M.J., 1983, "*A Numerical Solution for Layered Solid Contact Problems With Application to Bearings*," Journal of Lubrication Technology, Vol. 105, pp. 585-590.
8. King, R.B. and O'Sullivan, 1987, "*Sliding Contact Stresses in a Two-Dimensional Layered Elastic Half-Space*," International Journal of Solids and Structures, Vol. 23, No. 5, pp. 581-597.
9. O'Sullivan, T.C. and King, R.B., 1988, "*Sliding Contact Stress Field Due to a Spherical Indenter on a Layered Elastic Half-Space*," Journal of Tribology, Vol. 110, pp. 235-240.
10. Cole, S.J. and Sayles, R.S., 1992, "*A Numerical Model for the Contact of Layered Elastic Bodies With Real Rough Surfaces*," Journal of Tribology, Vol. 114, pp. 334-340.

11. Kuo, C.H. and Keer, L.M., 1992, "*Contact Stress Analysis of a Layered Transversely Isotropic Half-Space*," *Journal of Tribology*, Vol. 114, pp. 253-262.
12. Polonsky, I.A. and Keer, L.M., 2000, "*A Fast and Accurate Method for Numerical Analysis of Elastic Layered Contacts*," *Journal of Tribology*, Vol. 122, pp. 30-35.
13. Chudoba, T., Schwartz, N., and Richter, F., 2002, "*Step Towards a Mechanical Modeling of Layered Systems*," *Surface and Coatings Technology*, Vol. 154, pp. 140-151.
14. Komvopoulos, K., 1988, "*Finite Element Analysis of a Layered Elastic Solid in Normal Contact With a Rigid Surface*," *Journal of Tribology*, Vol. 110, pp. 477-485.
15. Komvopoulos, K., 1989, "*Elastic-Plastic Finite Element Analysis of Indented Layered Media*," *Journal of Tribology*, Vol. 111, pp. 430-439.
16. Bhattacharya, A.K. and Nix, W.D., 1988, "*Analysis of Elastic and Plastic Deformation Associated with Indentation Testing of Thin Films on Substrates*," *International Journal of Solids and Structures*, Vol. 24, No. 12, pp. 1287-1298.
17. Sun, Y., Bloyce, A., and Bell, T., 1995, "*Finite Element Analysis of Plastic Deformation of Various TiN Coating/Substrate Systems Under Normal Contact with a Rigid Sphere*," *Thin Solid Films*, Vol. 271, pp. 122-131.
18. Kral, E.R. and Komvopoulos, K., 1997, "*Three-Dimensional Finite Element Analysis of Subsurface Stress and Strain Fields Due to Sliding Contact on an Elastic-Plastic Layered Medium*," *Journal of Tribology*, Vol. 119, pp. 332-341.
19. Ye, N. and Komvopoulos, K., 2003, "*Effect of Residual Stress in Surface Layer on Contact Deformation of Elastic-Plastic Layered Media*," *Journal of Tribology*, Vol. 125, pp. 692-699.
20. Doerner, M.F. and Nix, W.D., 1986, "*A method for Interpreting the Data from Depth-Sensing Indentation Instruments*," *Material Research Society*, 1(4) Jul/Aug, pp. 601-609.
21. Pharr, G.M. and Oliver, W.C., 1992, "*Measurement of Thin Film Mechanical Properties Using Nanoindentation*," *MRS Bulletin*, July, pp. 28-33.
22. Page, T.F. and Hainsworth, S.V., 1993, "*Using Nanoindentation Techniques for the Characterization of Coated Systems: A Critique*," *Surface and Coatings Technology*, 61, pp. 201-208.
23. Knapp, J.A., Follstaedt, D.M., and Myers, S.M., 1996, "*Precipitate-Hardened Aluminum alloys Formed using Pulsed Laser Deposition*," *Journal of Applied Physics*, Vol. 79, Num 2, pp. 1116-1122.
24. Knapp, J.A., Follstaedt, D.M., Barbour, J.C., and Myers, S.M., 1997, "*Finite-Element Modeling of Nanoindentation for Determining the Mechanical Properties of implanted Layers and Thin Films*," *Nuclear Instruments and Methods in Physics Research B*, 127/128, pp. 935-939.
25. Knapp, J.A., Follstaedt, D.M., Myers, S.M., Barbour, J.C., and Friedmann, T.A., 1999, "*Finite-Element Modeling of Nanoindentation*," *Journal of Applied Physics*, Vol. 85, Num. 3, pp. 1460-1474.



26. Bouzakis, K.D., Michailidis, and N., Erkens, G., 2001, "*Thin Hard Coating Stress-Strain Curve Determination through a FEM Supported Evaluation of Nanoindentation Test Results,*" Surface and Coatings Technology, 142-144, pp. 102-109.